RUPRECHT-KARLS-UNIVERSITÄT HEIDELBERG

Elisabeth Kierig

Novel Control Algorithm for Real Time Adaptive Optics Systems

Diplomarbeit

HD-KIP-03-08

KIRCHHOFF-INSTITUT FÜR PHYSIK

Faculty of Physics and Astronomy

University of Heidelberg

Diploma thesis

in Physics

submitted by

Elisabeth Kierig

born in Frankfurt

2003

Novel Control Algorithm for Real Time Adaptive Optics Systems

This diploma thesis has been carried out by Elisabeth Kierig at the

Kirchhoff Institut für Physik

under the supervision of

Herrn Prof. Dr. Joseph Bille

Zusammenfassung

Neue stereotaktische neurochirurgische Verfahren ermölichen es Gehirntumore minimal invasiv zu entfernen und damit die Belastung des Patienten erheblich zu verringern. Die Qualität der zur Operationsüberwachung notwendigen in situ Bilder wird durch Spühlflüssigkeit und schon abgetragene Gewebeteile extrem beeinträchtigt. Diese Störungen sollen mit adaptiver Optik kompensiert werden, d.h. die auftretenden Aberrationen sollen in Echtzeit analysiert und korrigiert werden. Die erfolgreiche Entwicklung eines hierfür optimierten Kontrollalgorithmus für die Ansteuerung einen Membranspiegels wird in dieser Arbeit dargelegt. Des weiteren wird der Aubau eines geeigneten adaptiv opitschen Testsystems beschrieben.

Abstract

New sterotactic neurosurgical techniques enable a micro invasive treatment of brain tumors and therefore decrease the patients strain significantly. To allow for a precise ablation process high quality in situ pictures are essential. The quality of the in situ images is severely degraded due to irrigation liquid and ablated tissue. It is possible to correct for these aberrations employing adaptive optics. Therefore a real time realisation of a closed loop system containing detection, reconstruction and correction unit is desired. The design of an control algorithm to shape a membrane mirror, optimised for real time applications, is presented within this thesis. Furthermore the construction of an adaptive optics system suitable to test this algorithm is described.

Contents

Introduction

Optics is one of the classic disciplines of physics and imaging systems form a considerable part of it the . Here great efforts have been made to increase the quality on the 'hardware' side, like lenses and mirrors as well as light sources. Today's optics equipment reaches high precisions, mirror or lens surfaces can be produced with sub-micron accuracies as well as laser techniques deliver light sources of high homogeneity. Still there is an inconnu, which is turbulence, i.e. irregularities of the refractive index, in the propagation path. All this has already be foreseen by Sir Isaac Newton in his work about optics:

> If the Theory of making Telescopes could at length be fully brought into Practice, yet there would be certain Bounds beyond which Telescopes could not perform. For the Air through which we look upon the Stars, is in perpetual Tremor; as may be seen by the tremulous Motion of Shadows cast from high Towers, and by the twinkling of the fix'd Stars. But these Stars do not twinkle when viewed through Telescopes which have large apertures. For the Rays of Light which pass through divers parts of the aperture, tremble each of them apart, and by means of their various and sometimes contrary Tremors, fall at one and the same time upon different points in the bottom of the Eye, and their trembling Motions are too quick and confused to be perceived severally. And all these illuminated Points constitute one broad lucid Point, composed of those many trembling Points confusedly and insensibly mixed with one another by very short and swift Tremors, and thereby cause the Star to appear broader than it is, and without any trembling of the whole. Long Telescopes may cause Objects to appear brighter as to take away that confusion of the Rays which arises from the Tremors of the Atmosphere. The only Remedy is a most serene and quiet Air, such as may perhaps be found on the tops of the highest Mountains above the grosser Clouds.

Here a new discipline has come up to solve this problem. It was in 1953, that H.W. Babcock [1] published his idea to compensate for turbulence in the atmosphere by active optics devices like deformable mirrors. It still is the astronomical society that enforces the work on this field. With impressive pictures of high resolution they showed the effectiveness of this method. From a growing number

of adaptive optics systems the Very–Large–Telescope (VLT) [2] in Chile is the largest and most sophisticated setup. There even exist efforts to implement low cost systems for amateur astronomy [3]. Medicine is another field where adaptive optics is employed. It has successfully been applied to diagnostic instruments in ophtalmoloy. Currently scientists aim to utilise adaptive optics for endoscopic surgery. As the dimension of those optics systems is in the order of several centimeters, also the adaptive optics devices have to be of the same size.
The aim of this thesis is the implementation of a suitable control algorithm for such a small scale adaptive optics system. From earlier work one learned, that existing solutions were much to slow for this purpose. Therefore a suitable adaptive optics system had to be designed to test and optimise the new algorithm.

Chapter 1

Medical Applications of Adaptive Optics

In this chapter an overview of the up to date applications of adaptive optics systems is given.
In ophthalmology *retinal laser scanning tomography* images the retina by sensing the light emerging from the eye after reflection at the retina[4]. Those images are very helpful for early diagnoses of numerous diseases like glaucoma, but as the eye is no perfect optics system, their resolution is reduced by disturbances of the laser light. Static aberrations occur due to corneal imperfections, well known as they also affect the quality of human vision. Besides the human eye performs transient movements, while fixing a target, which is another source of aberration. Using adaptive optics it is possible to compensate for those aberrations and hence to increase the image quality to the diffraction limit. For instance A. Türpitz developed such a retinal laser scanning tomograph with included adaptive optics correction unit[5].
As mentioned before a current field of interest is the application of adaptive optics to the field of neurosurgery, to stereotactic neurosurgery, which is a micro invasive procedure, to be more precise. The method of stereotaxis was first invented by Victor Horsley and Robert Henry Clarke in 1904 to reach precisely subcortical points through the normal brain to treat moving disorder, pain, epilepsy or impairment of the limbic systems, more see[6]. The idea is to use a metal frame externally fixed to the patient's skull, to serve as reference for a three dimensional coordinate system. On the basis of images from preceding x–ray, computer–tomographic (CT) as well as nuclear magnetic resonance (NMR) examinations target points and volumes can be located precisely in this coordinate system. This supplies a navigation system for telecommanded surgical instruments inside the head[7] and therefore enables to treat deep seated tumors, while avoiding to remove greater parts of the skullcap.
The Department of Stereotactic and Functional Neurosurgery at the university of Cologne and the DKFZ (Deutsches Krebsforschungszentrum) in Heidelberg are

working on a project that combines this method with an ablation based clearance of cancerous tissue. The manner of interaction of a laser with tissue depends mainly on the power density and the duration of the irradiance, i.e. the amount of energy deposited in the area (see figure 1.1). Till today mainly so called 'thermally active' lasers are used to destroy tissue. These are for example CO_2 or Nd:YAG lasers. Their power density lies within the range of 10^4 W/cm^2, which leads to a warming and exceeding 60° C to a denaturing (Nd:YAG) or evaporation (CO_2) of the tissue. Problematic is, that a traumatisation of the surrounding tissue is unavoidable. Due to the deposition of large amounts of heat at the target volume, the surrounding tissue is also heated and therefore severely damaged. The depth of the damaged zone around the cleared out tumor depends on the power density, but it is at least several millimeters deep.
With the method of plasma–mediated ablation the amount of stray heat is significantly reduced. If the power density reach the range of $10^9 - 10^{12}$ W/cm^2, the emerging electric field generates a microplasma, which is a highly ionised unstable state. The tissue gets destroyed by ionisation as well as the shock wave induced by the expansion of the plasma. In first tests [7] no thermal side effects like coagulation, carbonisation or oedems appeared, the surrounding tissue was not affected. For more information about laser–tissue interaction see [8].
The probe employed by the Department of Stereotactic and Functional Neuro-

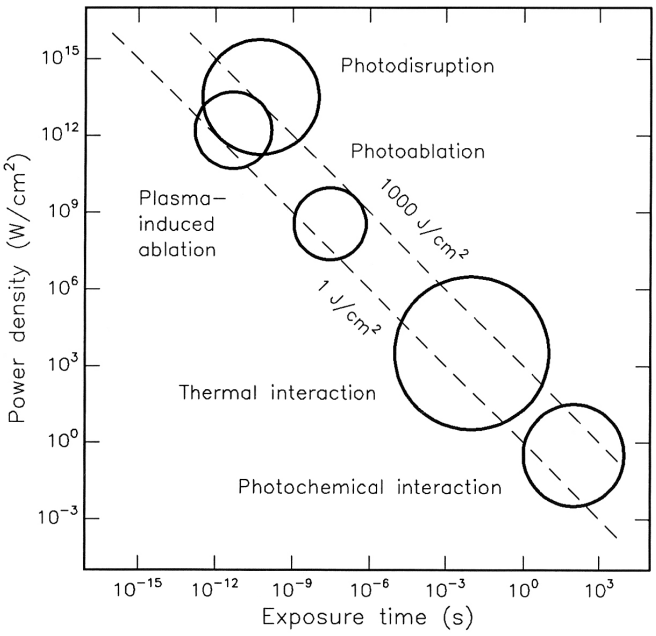

Figure 1.1: Dependence of laser–tissue–interaction on the power density.

surgery at the University of Cologne and the DKFZ guides two laser beams onto

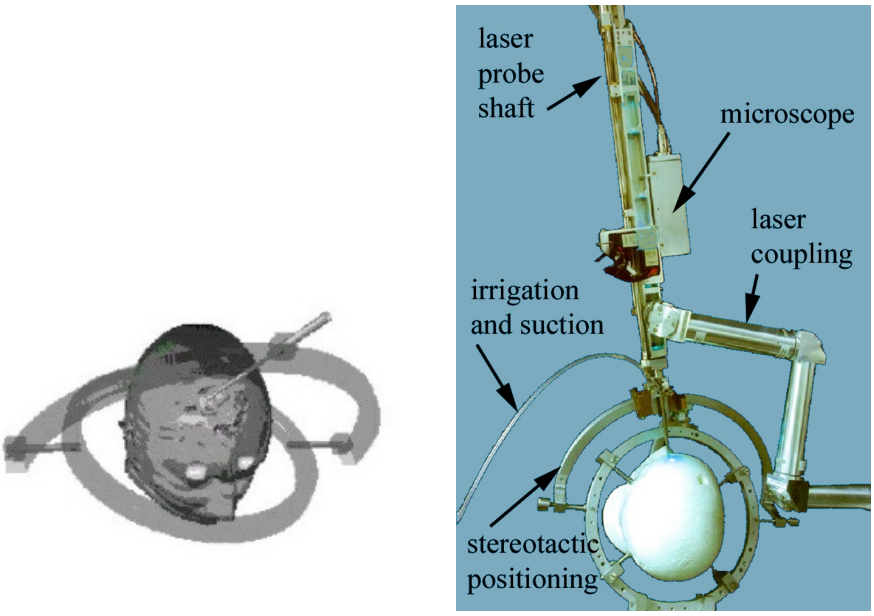

(a) (b)

Figure 1.2: Scheme (a) and photo (b) of the probe combined with the stereotactic ring.

the tissue, one for ablation and one for diagnostics. The laser for ablation is a Nd:YLF laser with ultra short pulses of some picosecond duration and a power density greater than 10^{11} W/cm^2. One pulse of this laser destroys a very small volume of about 8×10^5 μm^3, so that almost any target geometry can be cleared away by computer controlled scanning with repeated pulses. For diagnostics a cw–laser continuously scans the region of interest. In combination with a confocal microscope[9], in situ images of the operation area are obtained. The CT images give only an approximative position and size of the cancerous tissue. In combination with the in situ images the surgeon has the opportunity to selectively remove the cancerous and not the healthy tissue. The microscope designed for this purpose by K.Greger is a auto fluorescence microscope, accompanied with an improved image processing technique to distinguish between healthy and cancerous tissue[10]. This system is called OligoChannel Spectrum Analyzer (OCSA). A scheme and a picture of the probe fixed to the stereotactic frame are shown in figure 1.2.

The quality of the optical system inside the tool is of great importance. However it is restricted due to two main reasons. For once the diameter of the tool should be as small as possible and secondly the operation cavity is filled with liquid, as the ablated tissue is removed continuously by irrigation and suction through the laser probe. This liquid gets warmed erratic over the volume by the laser beams passing through. It thus becomes inhomogeneous and formes so called thermal

lenses due to local changes of the refractive index, aberrating the laser beams. Such disturbances reduce the beam quality of the cw laser and thus of the in situ images in the microscope, as well as the focus quality of the ablation laser beam. If the pulsed laser can not be focused to a small beam waist, the energy density might not reach the plasma threshold. Instead of ablated, the tissue would only get thermally damaged. Here adaptive optics can be applied to guaranty a precise ablation and clear in situ images. How such a surgical system including adaptive optics could be designed is shown in figure 1.3. How to control the active optics devise in real time shall be carried out in this work.

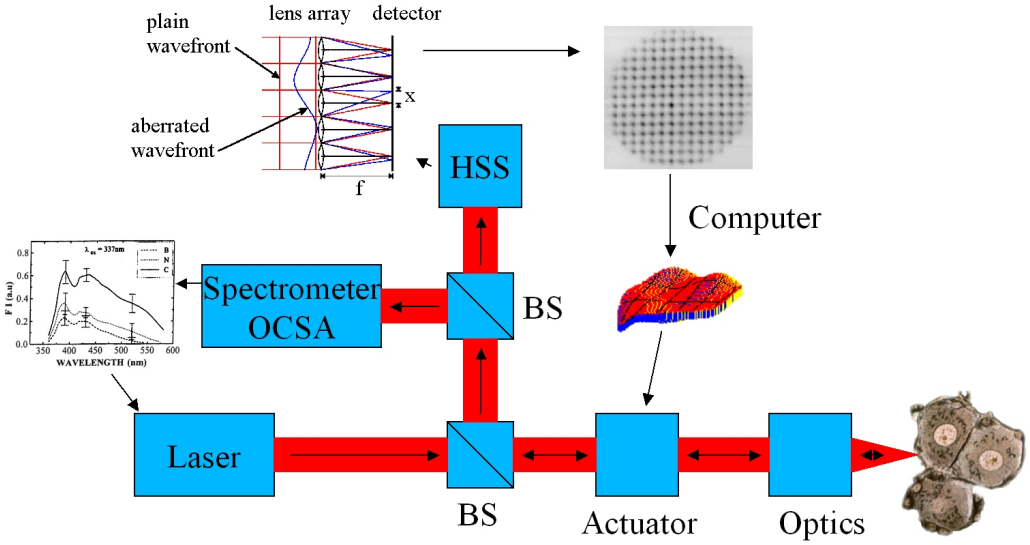

Figure 1.3: Layout of a surgical system including adaptive optics.

Chapter 2

Theoretical Foundation

In this chapter some specific terms concerning optics will be explained and the conceptual framework given for what is examined and done by adaptive optics.

2.1 Concept of Light as Wavefront

A light wave is a disturbance, comprising variations in space and time of coupled electric and magnetic fields and therefore obeys the Maxwell equations. As all applications described in the following do restrict themselves to a charge–free medium ($\rho = 0$) the Maxwell equations [11] for those systems are given by:

$$\nabla \cdot \vec{E}(\vec{r},t) = 0 \tag{2.1}$$

$$\nabla \cdot \vec{B}(\vec{r},t) = 0 \tag{2.2}$$

$$\nabla \times \vec{E}(\vec{r},t) = -\frac{\partial \vec{B}(\vec{r},t)}{\partial t} \tag{2.3}$$

$$\nabla \times \vec{B}(\vec{r},t) = \mu_0 \epsilon_0 \frac{\partial \vec{E}(\vec{r},t)}{\partial t}. \tag{2.4}$$

One important consequence of these equations is the wave equation, describing the propagation of an electromagnetic disturbance along a linear path in propagation direction, often called ray:

$$\nabla^2 \vec{E} - \mu_0 \epsilon_0 \frac{\partial^2 \vec{E}}{\partial t^2} = 0 \tag{2.5}$$

$$\nabla^2 \vec{B} - \mu_0 \epsilon_0 \frac{\partial^2 \vec{B}}{\partial t^2} = 0, \tag{2.6}$$

with the propagation velocity:

$$v = c = \frac{1}{\sqrt{\mu_0 \epsilon_0}}. \tag{2.7}$$

One solutions to equation (2.5) and (2.6) respectively, that also satisfy the Maxwell equations, is a plane wave:

$$E(\vec{r},t) = Re[E_0 \exp(i\phi(\vec{r},t))] = Re[E_0 \exp(i(\omega t - \vec{k}\cdot\vec{r}+\varphi))] \quad (2.8)$$
$$B(\vec{r},t) = Re[B_0 \exp(i\phi(\vec{r},t))] = Re[B_0 \exp(i(\omega t - \vec{k}\cdot\vec{r}+\varphi))], \quad (2.9)$$

E_0, B_0: amplitude,
ω: wave frequency,
k: wave vector.

If such a plane wave passes through a convex lens, it collapses in one point, called focus point. The distance of this point to the lens is the lens' focal length. As an imaging system is a combination of lenses and the image of a point source is again a point. This point is also referred to as image point or conjugated point. Conjugated plane is another name for the image plane, that contains all image points of an object, while maintaining the objects aspect ratio. Another name for a plane wave is collimated beam, it indicates that the beam comes from a point source infinitely far away and therefor can be described as being plane.
Another solution for the equations (2.5) and (2.6) is a spherical wave:

$$E(\vec{r},t) = Re[\frac{E_0}{r} \exp(i(\omega t - \vec{k}\cdot\vec{r}+\varphi))] \quad (2.10)$$
$$B(\vec{r},t) = Re[\frac{B_0}{r} \exp(i(\omega t - \vec{k}\cdot\vec{r}+\varphi))], \quad (2.11)$$

which is the form of a wave emerging from a point source. As according to Huygens' principle any source can be described as superposition of many point sources, the spherical solution will be the most frequently used model of light.
Concerning imaging systems the most interesting quantity in the above expressions is the phase ϕ. Constant ϕ gives a surface of constant optical path length (OPL = length$\times$ refractive index) from the source, carrying all information about this source and therefore forming the image. Any imaging error can be described in terms of aberration of this phase front, concrete the optical path difference (OPD) $W(x,y)$, between an ideal wavefront, serving as reference wavefront, and the aberrated one. For a spherical wavefront, this is illustrated in figure 2.1.

In mathematical form this OPD function can be represented by a polynomial, so that every term describes a specific type of aberration, like tilt or defocus, and to which extend it is present. This is called a modal representation, in contrast to local ones, where each point of the OPD function is described independently by some absolute value. Most frequently used for modal representation is the Zernike polynomial series[12]. In polar coordinates (ρ,θ) it has the form:

$$Z_n^m(\rho,\theta) = \begin{cases} R_n^m(\rho)\ \cos(m\theta) & \text{for } m > 0 \\ R_n^{-m}(\rho)\ \sin(m\theta) & \text{for } m < 0 \\ R_n^m(\rho) & \text{for } m = 0, \end{cases} \quad (2.12)$$

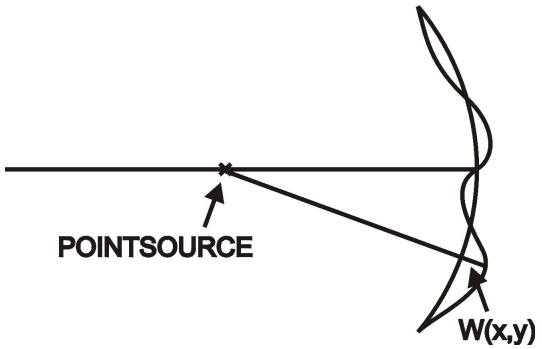

Figure 2.1: The aberration of a spherical wavefront can be measured as optical path difference $W(x, y)$ compared to an undisturbed spherical wavefront.

with

$$R_n^m(\rho) = \sum_{s=0}^{(n-m)/2} \frac{(-1)^s (n-s)!}{s!\,[(n+m)/2-s]!\,[(n-m)/2-s]!} r^{n-2s}, \qquad (2.13)$$

n: radial order,
m: azimuthal order, $m < n, (n-m)$ is even.

This polynomial set is normalised on a unit circle and its first terms depict just commonly known aberrations like tilt, defocus, astigmatism or coma, which makes it very illustrative (see figure 2.2). Therefore it is traditionally used for optical systems. There exist different numberings for the terms of the series, like an ISO representation, which is implemented in the interferometer software (see section 4.1.3) and the mirror control program I wrote or one by Malacara, used by T. Nirmaier in his sensor control program (see section 4.3). Generally in Cartesian coordinates the Zernike polynomials are linear combinations of Taylor monomials, a feature I will use for the wavefront reconstruction. The first 19 polynomials of the ISO representation are listed in table 3.1. Any OPD function can then be written as infinite sum of those Zernike polynomials with specific coefficients c_i:

$$W(x, y) = \sum_{i=0}^{\infty} c_i Z_i. \qquad (2.14)$$

Chromatic aberrations are not of interest here as only monochromatic light sources - lasers with well defined wavelength - are involved in this work.

2.2 Limits of Imaging Systems

Any imaging system aims to give a perfect image of some object in the image plane. Thus ideally all the light coming from the image should reach the image

plane undisturbed. But not even theoretically this is possible. As all optics devices, like a lens for example, are of finite size, diffraction effects at the edges degrade the propagation process and thus the image. Those effects are inherent in the Maxwell equations, so that the best one can do is to reach the limit of diffraction for an optics system. The interaction of light with optics devices on its way of propagation can in a strict mathematical derivation from Maxwell equations be described by the Helmholtz–Kirchhoff–theorem in full detail given in [13]. An approximation to this theorem, describing the light source as a sum of point sources and replacing the field distribution in the aperture plane with the incoming field, is summoned in Kirchoff's formula of propagation. Due to this the field E at a point (ρ, θ) in the plane normal to the direction of propagation and behind the aperture is given in polar coordinates by:

$$\vec{E}(\rho,\theta) = C\frac{e^{i(\omega t - k\vec{R})}}{\vec{R}} \int_{q=0}^{a}\int_{\Theta=0}^{2\pi} \underbrace{e^{i(\frac{k\rho q}{\vec{R}})\omega s(\theta-\Theta)}}_{E_{ap}(q,\Theta)} q \,\mathrm{d}q \,\mathrm{d}\Theta, \tag{2.15}$$

z: distance to aperture plane,
C: constant,
E_{ap}: field distribution in the aperture plane,
$\vec{R}$: vector from (ρ, θ) to (q, Θ),

where ap indicates, that the integral runs over the aperture, the light interacts with.
A concrete effect of diffraction on the image is, that a diffraction limited system does not focus a point source onto one single image point, but into a finite sized spot in the focus plane. This lateral intensity distribution is called the point spread function (PSF) of the system (see figure 2.3). The distance between its central maximum and the first zero is used to define the radius of a disk, which is called **Airy disk** after the British astronomer Sir George Bidell Airy. The size of the Airy disk is used to define a comparable measure of a focal point's size. It is approximately the size recognised by a human eye. The diameter is defined by:

$$d_{Airydisk} = 2.44\lambda(f/\sharp), \tag{2.16}$$

$f/\sharp$: F–number.

The **F-number** of a system is (effective) focal length F divided by entrance pupil diameter D, which e.g. for a biconvex lens is just the lens diameter:

$$f/\sharp \equiv \frac{f}{D}. \tag{2.17}$$

It is a measure for the effective light output of an optics system in the focus plane and therefore frequently used in medical applications to verify the doses, that can

be applied for example in eye operations.
Other limits of resolution are imperfections of optics instruments and light sources. A magnitude for the quality of the optics devices and there adjustment involved in am imaging system is the relative intensity deviation on axis, called **Strehl ration** or normalised intensity S. It is the quotient of the ideal intensity on axis and the real intensity on axis:

$$S = \frac{I(P)}{I_{\phi=0}} = \frac{1}{\pi^2} \mid \int_0^1 \int_0^{2\pi} e^{i[k\phi - v\rho\cos(\theta-\psi) - \frac{1}{2}u\rho^2]} \rho \, d\rho \, d\theta \mid, \tag{2.18}$$

where P is the point of intersection between wavefront and image plane and (ρ, θ) are points in the image plane. Problematic is that if tilt aberration is present the axis of the real wavefront is normal to the plane of that tilt and not parallel to the axis of the ideal intensity, so that the intensity distributions are shifted relative to each other in the image plane. Therefore the Strehl ration is only a figure of merit for the quality of beam propagation in a system, as long as static tilt is removed.
Concerning the light intensity there is another measure, that is interesting, when light sensitive surfaces, like the eye's retina or thin membrane mirrors are involved. This is the **optical load** E_E, which gives the light output in the image plane in form of load of radiation per area:

$$E_E = \frac{\mathrm{d}\Phi_e}{\mathrm{d}A_E} = \frac{I\mathrm{d}\Omega}{\mathrm{d}A_E}, \tag{2.19}$$

Φ_e: power of radiation (of source),
Ω: angel of space,
A_E: irradiated area, i.e. image plane.

Pleas refer to [14, 15] for further reading on optics and adaptive optics.

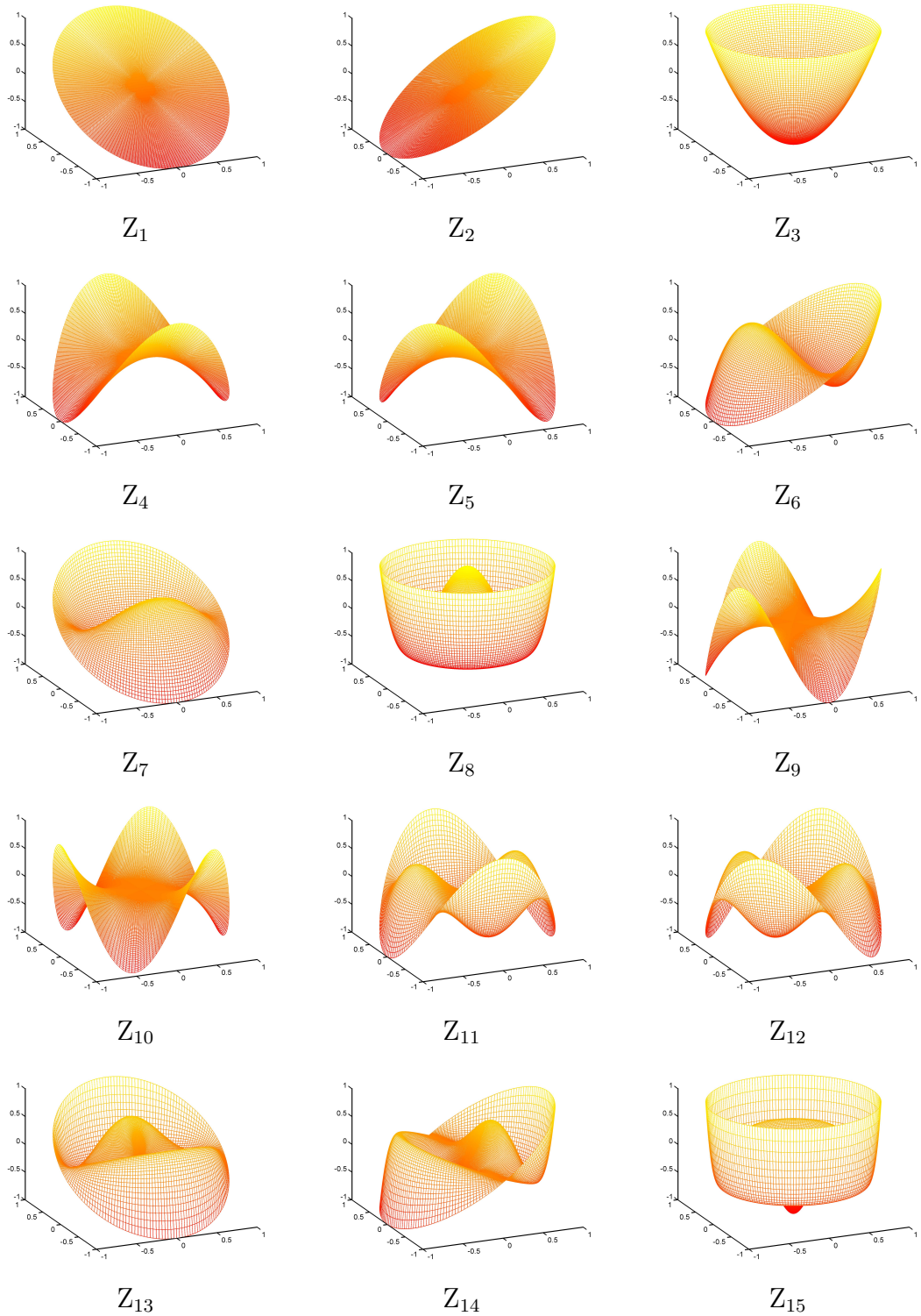

Figure 2.2: The first 15 Zernike coefficients, according to ISO numbering.

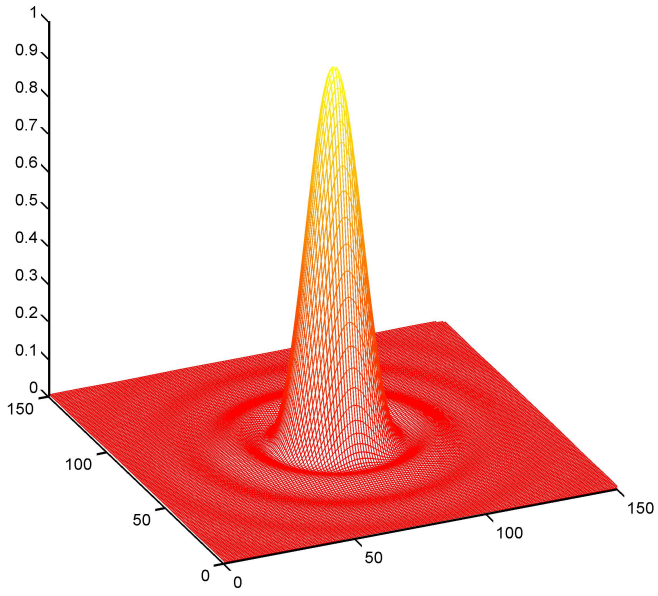

Figure 2.3: The point spread function gives the lateral intensity distribution of an optics system at the focal plane.

Chapter 3

Adaptive Optics Systems

The theoretical foundations of adaptive optics were laid in the previous chapter. This chapter will introduce the principles of adaptive optics systems and give an overview of the current implementations.
An adaptive optics system is generally a system with some mechanical device, to compensate for imaging errors corresponding to disturbances in the propagation path. Such a system consists of three main units, a wavefront sensor, a wavefront reconstructor and a wavefront corrector, merged in a servo loop and driven in a frequency range up to 1 kHz. The wavefront sensor measures the optical path difference W or its gradient dW at a finite number of points across the exit pupil, passes this data to the reconstructor computer, which controls the wavefront corrector. A scheme of a whole system is shown in figure 3.1
Active optics systems are based on the same concept, but only aim to correct for slower quasi static errors. For example thermal telescope errors can be corrected with regulation rates of only about 0.01 Hz. Those errors occur due to the thermal expansion and contraction of the telescope mirrors and mounts. As the temperature changes during 24 h the telescope has to follow with its thermal load.
The following sections will focus on the three main units of an adaptive optics system.

3.1 Wavefront Sensing Techniques and Reconstruction

There are mainly three ways to measure wavefront aberrations. Either one uses interference, geometrical effects or intensity variations.

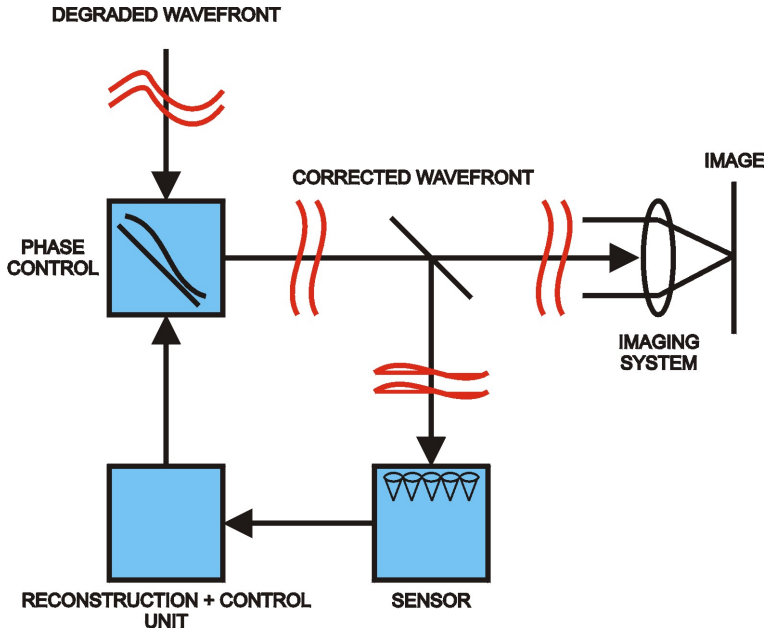

Figure 3.1: Scheme of an adaptive optics system.

3.1.1 Interference Based Wavefront Sensors

Interfering the aberrated wavefront with a reference wavefront, that resembles the undisturbed ideal wavefront, the fringe pattern reflects the phase shift between the two surfaces.
The correlation between phase shift δ for a certain wavelength λ and OPD W is generally given by:

$$\delta = \frac{4\pi W}{\lambda}. \tag{3.1}$$

There are many different ways to obtain a reference. Either it can be obtained from an external source or it must be generated from the aberrated wavefront itself. Examples for the latter are the radial shear interferometer and the point diffraction interferometer.
Generally high accuracies can be reached with interferometers, but disadvantages are, that they only work for coherent light sources, they are sensitive to vibration of the aperture and that they often need movable parts.

Radial Shear Interferometer

The radial shear interferometer is based on a Mach-Zehnder-type interferometer[14]. As can be seen in figure 3.2 the wavefront to be tested is parted by a beam splitter into a reference and a test arm. Each arm runs through a telescope before being

reunited. The reference arm gets expanded, the test arm compressed. That way the phase shift of the reference arm, in the region of the image plane, where the two beams overlap, is about a tenth wavelength or less[16], which is plane enough to be used as reference wavefront. By detecting the fringe pattern in the image plane, the interferometer becomes a sensor.

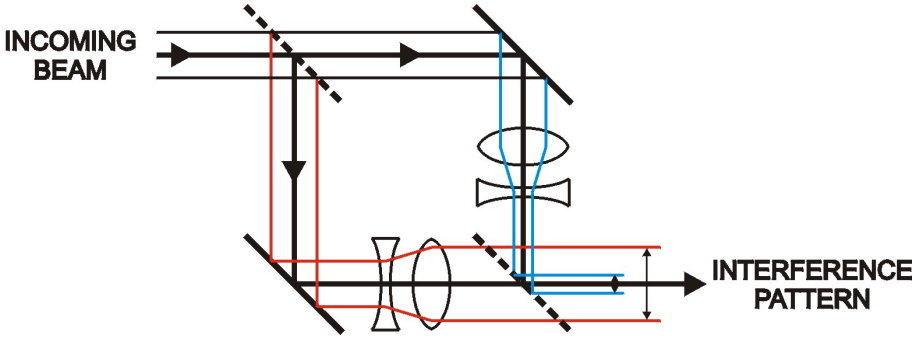

Figure 3.2: Radial shear interferometer

Point Diffraction Interferometer

The point diffraction interferometer, first build by Dr. Ray Smartt[17], is illustrated in figure 3.3. It is a neutral density filter disk with a small pinhole, which acts as diffraction aperture. Only a minute part of the beam interacts with it, being diffracted into a clean spherical wavefront. This serves as reference for the rest of the beam, that passes through unhindered except for a reduction in intensity. As the intensity distributions of the two interfering wavefronts diverge with increasing distance to the center, the fringe contrast goes down at the range extremes.

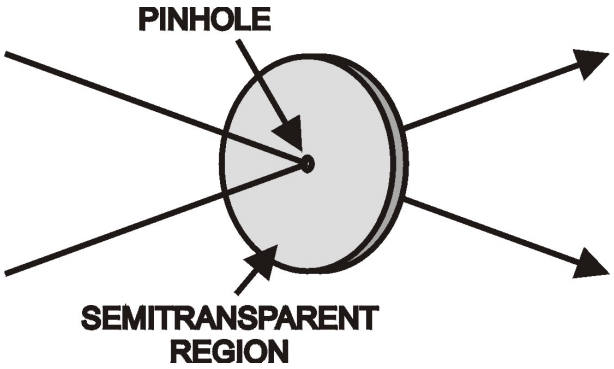

Figure 3.3: Structure of a point diffraction interferometer.

3.1.2 Intensity Based Wavefront Sensors

Knife Edge Test Principle

In the 19th century the French physicist Foucault showed that the form of a wavefront can be tested using a knife edge. A sharp edge, like a knife edge, is placed in the focus plane of the entrance pupil. It can be moved up and down in this plane. As an undisturbed wavefront converges to a point focus, the wavefront image on an observation screen well outside of the focal region will be completely blocked the moment the knife edge crosses the focal point. Aberrated wavefronts do not converge to a point focus, but the image formed is spread out around the ideal focus point instead. Hence the image in the focal plane is of finite size and can't be blocked out at once, but a straight shadow edge moves over the image.

Implementations

So called knife edge wavefront sensors use this method operating with one or more knife edges. The knife edge position is triggered together with intensity profiles of the pupil image. After the blades have passed the image the whole data is analysed by a computer and the optical path difference $W(x, y)$ is computed. Obviously here lies the main disadvantage of this sensing method. A lot of data analysis and calculation has to be done. Thus for high frequency rates great computer capacity is needed.
Also based on Foucault's idea is the pyramid wavefront sensor developed by the Italian astronomer Ragazoni. The incoming wavefront is focused onto the apex of a transparent four-sided pyramid. The expanding light inside the pyramid get diffracted by the four different sides onto four separate images below the pyramides base. In the ideal case the intensity is equally distributed among the four spots. This is obviously not the case for an aberrated wavefront. On the bases of the intensity distribution between these four pictures the optical path difference $W(x, y)$ can be determined.

Curvature Sensor

Another frequently used example of an intensity based wavefront sensor is the curvature sensor. Its method has first been proposed by F. Roddier *et al.*. Here the irradiance profiles in two complimentary planes in the same distance before and behind the focal plane of a perfect lens are detected. For a plane wavefront incident upon the lens the intensity is distributed symmetrically around the focus point. An aberrated wave does not converge onto the focal point and therefore the intensities measured in the two planes are different. The phase ϕ is related to the irradiance $I(\vec{r})$ by[15]:

$$\frac{I_1(\vec{r}) - I_2(-\vec{r})}{I_1(\vec{r}) + I_2(-\vec{r})} = \frac{f(f-s)}{s}[\nabla^2\phi(\frac{f}{s}\vec{r}) - \frac{\partial}{\partial\vec{n}}\phi(\frac{f}{s}\vec{r})\delta_c] \tag{3.2}$$

I_1: intensity on axis in the distance $\vec{r}$ before the focal point,
I_2: intensities in $-\vec{r}$ behind the focal point,
δ_c: Dirac delta function, representing the outward pointing normal derivatives on the edge of the signal.

3.1.3 Wavefront Sensors Based on Geometry

This class of wavefront sensors is based on pure ray optical considerations, which are valid as far as diffraction effects are negligible, i.e. the the aperture size is much bigger then the used wavelenght. A widely used exponent is the Hartmann-Shack-Sensor , which is an advancement of the Hartmann-Test(figure 3.4), which was originally developed by Hartmann for lens evaluation. For this test the wavefront falls paraxial onto a disk with a small circular hole. This disk, positioned in the entrance pupil of a lens, can be moved orthogonally to the optical axis. For different disk positions one detects the corresponding positions of the ray, that passes the hole, in the image plane. For a plane wavefront all rays reach the detector at the paraxial focal point. For aberrated wavefronts different rays reach the detector plane in different positions off-axis. These deviations T_x, T_y from the paraxial focal point provide all information about the local optical path difference $W(x, y)$ of the wavefront.

$$\frac{\partial W(x,y)}{\partial x} = -(\frac{nR}{r})T_x \tag{3.3}$$

$$\frac{\partial W(x,y)}{\partial y} = -(\frac{nR}{r})T_y \tag{3.4}$$

R: pupil radius
r: distance of exit pupil to focal plane
n: refractive index

An easy extension is the parallel Hartmann sensing. Instead of one hole, an

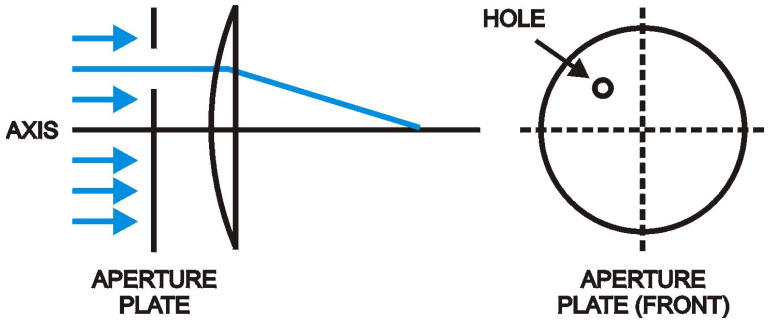

Figure 3.4: Illustration of the Hartmann–Test.

array of holes is printed on the aperture disk. As the $T_{x,y}$ values over the entire pupil would be present concurrently, the specific spots wouldn't be distinguishable. This is solved by the integration of lenses in each hole combined with a position sensitive detector in the focal plane. Finally leading to the Hartmann-Shack-Sensor, which leaves out the disk and instead fills the plane continuously with lenses to get as many spots as possible over the wavefront's cross section, consists only of a lenslet array and the detector.

Detection

Position sensitive detectors are in this group realised in two different ways. The simpler detector is based on a ccd[1] camera in combination with a computer based read out and an image analysis software. The more advanced detector is realised with an asic[2][18]. The latter detector was used in this work and is fully described in section 4.1.2.

Reconstruction

In the following paragraph it will be shown how to derive the OPD function out of the focus point positions measured by the sensor for each microlens. This is often referred to as direct approach of reconstruction in contrast to an indirect approach, that never works out the wavefront explicitly, but translates the measured local tilt information directly into signals for the control unit.
The deviation of each spot detected in the focal plane to the ideal focal spot position separately in x– and y–direction is $x_{measured} - x_{ideal} = \Delta x$ and $y_{measured} - y_{ideal} = \Delta y$. The correlation to the local tilt of the OPD W(x,y) is illustrated in figure 3.5 and given for the n*th* subaperture by:

$$\frac{\partial W(x_n, y_n)_{measured}}{\partial x} = \tan\alpha = \frac{\Delta x_n}{f} = P_n \tag{3.5}$$

$$\frac{\partial W(x_n, y_n)_{measured}}{\partial y} = \tan\beta = \frac{\Delta y_n}{f} = Q_n \tag{3.6}$$

f: focal length of the lenses,
α, β: angles between tilt and normal in x– and y–direction respectively.

The aim is now to find the OPD $W(x, y)$ (2.14), that fits best this measured deviations. This can be reached doing a least square fit, i.e. minimising the sum D of the squared deviations between wavefront derivatives and measured tilt for all N subapertures. This sum is:

$$D = \sum_{n=1}^{N} (\frac{\partial}{\partial x} W(x_n, y_n) - P_n)^2 + \sum_{n=1}^{N} (\frac{\partial}{\partial y} W(x_n, y_n) - Q_n)^2. \tag{3.7}$$

[1]CCD is the abbreviation for charged coupled device.
[2]ASIC is the abbreviation for application specific integrated circuit

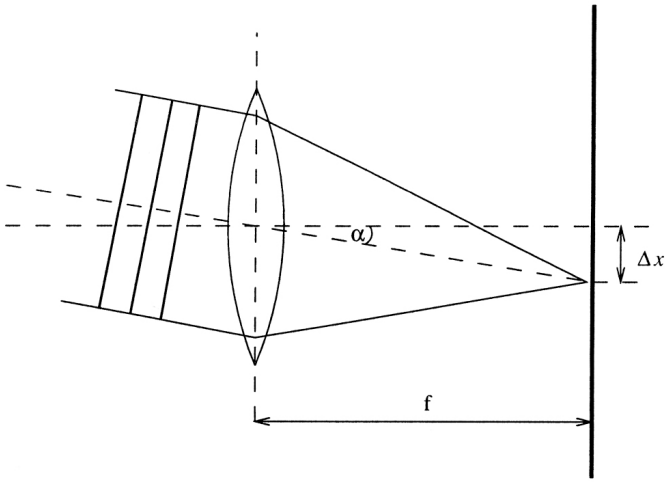

Figure 3.5: Correlation of focus point deviation in off axial direction and local tilt. This is also in the orthogonal direction the case.

If the wavefront derivatives are represented by a polynomial series, the fit parameters are the polynomial coefficients.

$$\frac{\partial W(x,y)}{\partial x} = \sum_i k_i L_i \tag{3.8}$$

$$\frac{\partial W(x,y)}{\partial y} = \sum_i l_i L_i, \tag{3.9}$$

where L_i are some not yet specified polynomials and k_i, l_i the free fit parameters. Now the sum D reaches its minimal value, if the derivatives concerning k_j and l_j vanish, meaning:

$$0 = \frac{\partial D}{\partial k_j} = 2\sum_{n=1}^{N}(\sum_i k_i L_i(x_n,y_n) - P_n)L_j(x_n,y_n) \tag{3.10}$$

$$0 = \frac{\partial D}{\partial l_j} = 2\sum_{i=1}^{N}(\sum_i l_i L_i(x_n,y_n) - Q_n)L_j(x_n,y_n) \tag{3.11}$$

$$\Rightarrow \sum_{n=1}^{N} P_n L_j(x_n,y_n) = \sum_i k_i \sum_{n=1}^{N} L_i(x_n,y_n)L_j(x_n,y_n) \tag{3.12}$$

$$\sum_{n=1}^{N} Q_n L_j(x_n,y_n) = \sum_i l_i \sum_{n=1}^{N} L_i(x_n,y_n)L_j(x_n,y_n) \tag{3.13}$$

This simplifies considerably, if an orthogonal set of polynomials for L_i is chosen, so that

$$\sum_{n=1}^{N} L_i(x_n, y_n) L_j(x_n, y_n) = \delta_{ij} \quad \forall\, i, j, \tag{3.14}$$

δ_{ij}: Kronecker symbol.

Hence the conditions for minimisation become:

$$k_j = \frac{\sum_{n=1}^{N} P_n L_j(x_n, y_n)}{\sum_{n=1}^{N} L_j^2(x_n, y_n)}, \tag{3.15}$$

$$l_j = \frac{\sum_{n=1}^{N} Q_n L_j(x_n, y_n)}{\sum_{n=1}^{N} L_j^2(x_n, y_n)}. \tag{3.16}$$

From these fitted wavefront derivatives, the wavefront itself must be determined. Therefore a Taylor monomial representation for the wavefront $W(x, y)$ is selected, because these monomials are less complex than the Zernike polynomial series and it is easy to derive the latter from them later on (see chapter 2). The wavefront then is:

$$\begin{aligned} W(x, y) = a_0 + a_1 x + a_2 y + a_3 x^2 + a_4 xy + a_5 y^2 + a_6 x^3 \\ + a_7 x^2 y + a_8 x y^2 + a_9 y^3 + a_{10} x^4 + a_{11} x^3 y + \ldots, \end{aligned} \tag{3.17}$$

and its partial derivatives become:

$$\frac{\partial}{\partial x} W(x, y) = a_1 + 2a_3 x + a_4 y + 3a_6 x^2 \ldots + a_{13} y^3 \tag{3.18}$$

$$\frac{\partial}{\partial y} W(x, y) = a_2 + a_4 x + 2a_5 y + a_7 x^2 \ldots + 4a_{14} y^3, \tag{3.19}$$

with an accuracy to the third order. Now the Taylor coefficients can easily be determined by comparing them to the fitted derivatives from above:

$$a_1 + 2a_3 x + a_4 y + 3a_6 x^2 \ldots + a_{13} y^3 = k_1 L_1 + k_2 L_2 + \ldots + k_i L_i, \tag{3.20}$$

$$a_2 + a_4 x + 2a_5 y + a_7 x^2 \ldots + 4a_{14} y^3 = l_1 L_1 + l_2 L_2 + \ldots + l_i L_i. \tag{3.21}$$

As the cartesian representation of all Zernike polynomials is based on linear combinations of the Taylor monomials, all Zernike coefficients can easily be calculated. A detailled description of the way how this is done in can be found in[19]. All the other polynomials and the concrete coefficients are listed in appendix A.

3.2 Wavefront Correction

Active optics elements are used to correct a wavefront, i.e devices that can change the wavefront's phase in a controlled manner. There are two ways to do this, either in transmission by changing the light velocity, i.e. the refractive index, or in reflection by mechanical changes of the optical path length.

Order	n	m	Coefficient	Polynomial	Significance
0	0	0	Z_0	1	offset(piston)
2	1	1	Z_1	$\rho\ cos\ \theta$	tilt x
			Z_2	$\rho\ sin\ \theta$	tilt y
	2	0	Z_3	$2\ \rho^2 - 1$	defocus
4	2	2	Z_4	$\rho^2\ cos\ 2\theta$	astigmatism 0°, $1st$
			Z_5	$\rho^2\ sin\ 2\theta$	astigmatism 45°, $1st$
	3	1	Z_6	$(3\rho^2 - 2)\ cos\ \theta$	coma and tilt, x
			Z_7	$(3\rho^2 - 2)\ sin\ \theta$	coma and tilt, y
	4	0	Z_8	$6\rho^4 - 6\rho^2 + 1$	spherical aberration
6	3	3	Z_9	$\rho^3\ cos\ 3\theta$	trifoil, 0°
			Z_{10}	$\rho^3\ sin\ 3\theta$	trifoil, 30°
	4	2	Z_{11}	$(4\rho^2 - 3)\ \rho^2\ cos\ 2\theta$	astigmatism 0°, $2nd$
			Z_{12}	$(4\rho^2 - 3)\ \rho^2\ sin\ 2\theta$	astigmatism 45°, $2nd$
	5	1	Z_{13}	$(10\rho^4 - 12\rho^2 + 3)\ cos\ \theta$	
			Z_{14}	$(10\rho^4 - 12\rho^2 + 3)\ sin\ \theta$	
	6	0	Z_{15}	$20\rho^6 - 30\rho^4 + 12\rho^2 - 1$	radial term
8	4	4	Z_{16}	$\rho^4\ cos\ 4\theta$	tetrafoil, 0°
			Z_{17}	$\rho^4\ sin\ 4\theta$	tetrafoil, 22.5°
	5	3	Z_{18}	$(5\rho^2 - 4)\ \rho^3\ cos\ 3\theta$	
			Z_{19}	$(5\rho^2 - 4)\ \rho^3\ sin\ 3\theta$	

Table 3.1: Zernike polynomials in ISO nomenclature.

3.2.1 Transmission Light Elements

Phase changes in transmission can be realised by liquid crystals (LC). Other than in frequently used LC displays phase modulators do not change the intensity, but the phase of the transmitted light. This can be controlled dynamically, allowing closed–loop operations in the kHz range. Advantages are a large stroke range of tens of wavelength , small consumed capacities (0.1 mW/cm^2), compact design, no–moved parts, the wide interval of working temperatures (-20°c to 100°C), low cost of initial materials as well as that only low voltages are needed for control [20, 21].

3.2.2 Mirrors

With active mirrors one can change the optical path length of a wavefront. There are many different realisations of such devices, but the principle of the correction mechanism is always the same. If the wavefront has an OPD of W, the mirror has to be deformed by $W/2$, so that the aberrations are cancelled out after reflection, as it is illustrated in figure 3.6.

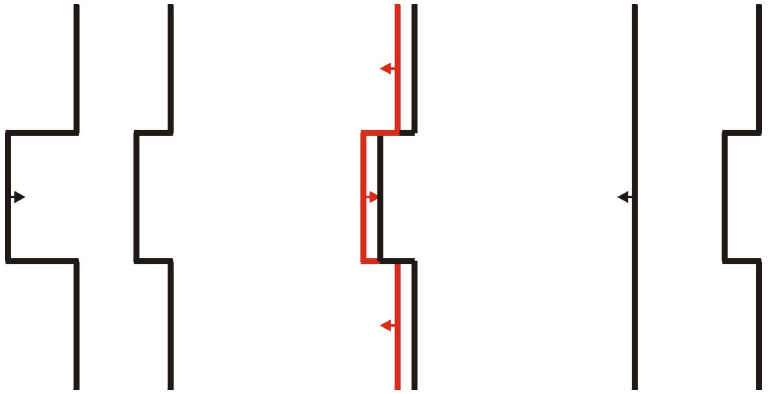

Figure 3.6: Principle of wavefront correction with active mirror.

Segmented Mirrors

The mirror surface of segmented mirrors is a combination of closely set mirror segments, which are usually hexagonal shaped. In simpler implementations each segment has only one degree of freedom, i.e. it can be moved up and down. So called tip–tilt–mirrors open additional degrees of fredom for each segment. The segments can be moved up and down, as they are supported by tip and can be tilted in two directions due to actuators (see figure 3.7).
As the outline of those mirrors is comparable to the Hartmann-Shack sensor's

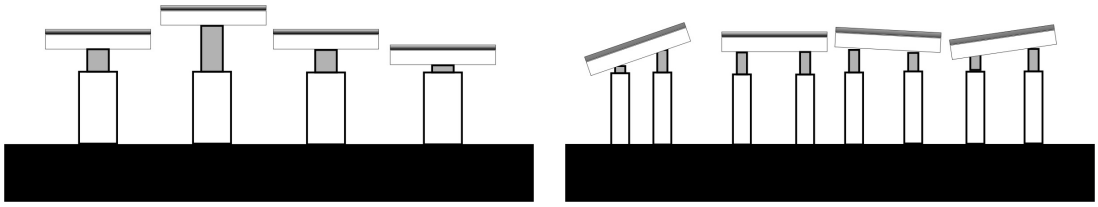

Figure 3.7: Sketch of tip and tip–tilt realisation of segmented mirrors.

segmentation, the control of the actuators is more straight forward. Each mirror segment adjusts its declination directly to the data of the local slope of the correspondent micro lens.
What is generally problematic about segmentation, is to synchronise the piston of each mirror to its neighbours to guarantee a smooth wavefront. Another handicap are the gaps between the discrete mirror segments, that cause a loss of information as well as diffraction of light. The advances in micro machining allow the miniaturisation of the segmented mirrors. This new class of segmented mirrors are the micromachine–electromechanical (MEM) deformable mirrors. On a silicon or metal substrate components like very small mechanically functioning actuators and mirrors are micromachined. In addition control and detection electronics can also be integrated to such devices. Current technologies allowes to have up to 10^5 actuators in one device [22, 15]. The disadvantage of segmented mirrors described above hold also for the micro machind ones. Here the fitted control electronics causes even further separation of the mirror segments.

Continuous Mirrors

Bimorph Mirrors The basic unit of bimorph mirrors[23] is a passive layer attached to two counter acting layers of piezoelectric material. Responding to a control voltage the piezoelectric layers expand and cause a bending of the layered structure. This local curvature is directly proportional to the applied voltage. An array of control electrodes underneath the piezoelectric layers enables to control the bending of the face sheet locally. Like the segmented mirrors matched the geometry of the Hartmann–Shack–Sensors, the geometrically corresponding sensor for bimorph mirrors are the curvature sensors. In contrast to segmented mirrors here the reflected wavefronts inherently are continuous.

Membrane Mirrors A membrane mirror is basically a thin flexible membrane, typically 0.5 - 1.5 μm thick, coated with some reflecting material, that is situated over an array of actuators. An examples for an implementation is sketched in figure 3.8. The actuators can be mechanical devices forcing the face-sheet to bend by pushing it up or pulling it down. More commonly the interacting force is electrostatically. Than the actuators are electrodes and the membrane is pulled

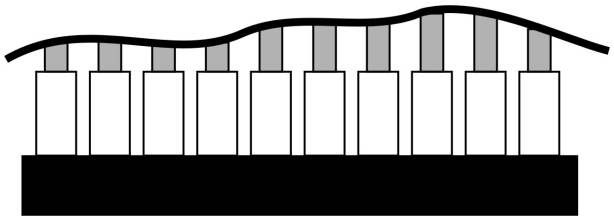

Figure 3.8: Membrane mirror with mechanical actuators.

towards them by electrostatic attraction. This enables only one direction of deformation if the membrane is grounded. Therefore is helpeful to pre-bias the membrane mirror. The force, produced by each electrode in this case is:

$$F = \frac{\epsilon\epsilon_0(V_b + V_c)^2 A}{d^2}, \tag{3.22}$$

where V_b is the bias voltage, V_c the control voltage, A the surface of one electrode and d the distance between electrode and membrane. As the sensitivity to the control voltage V_c is equal to:

$$\frac{dF}{dV_c} = \frac{2\epsilon\epsilon_0(V_b + V_c)}{d^2} \approx \frac{2\varepsilon\varepsilon_0 V_b A}{d^2}, \tag{3.23}$$

it is roughly proportional to the bias voltage, what implies, that to bias the mirror also enables to use smaller control voltages, than without bias and the mirror could even be driven by standard low-voltage integrated electronics. To reconstruct specific surfaces with the mirror it is important to understand the relation between stroke and the applied voltage distribution. Unfortunately the electrodes are not independent of each other. The voltage applied to one electrode also affects the neighbouring, so that the description of the mirror surface as sum of individual actuator activities can only be an approximation. In addition one has to bare in mind, that an elastic membrane, which is deformed by the actuators, always fulfills the membrane equation. In conclusion, the membrane can not be arbitrarily shaped.

Chapter 4

Implementation

4.1 Technical Data

4.1.1 Experimental Setup

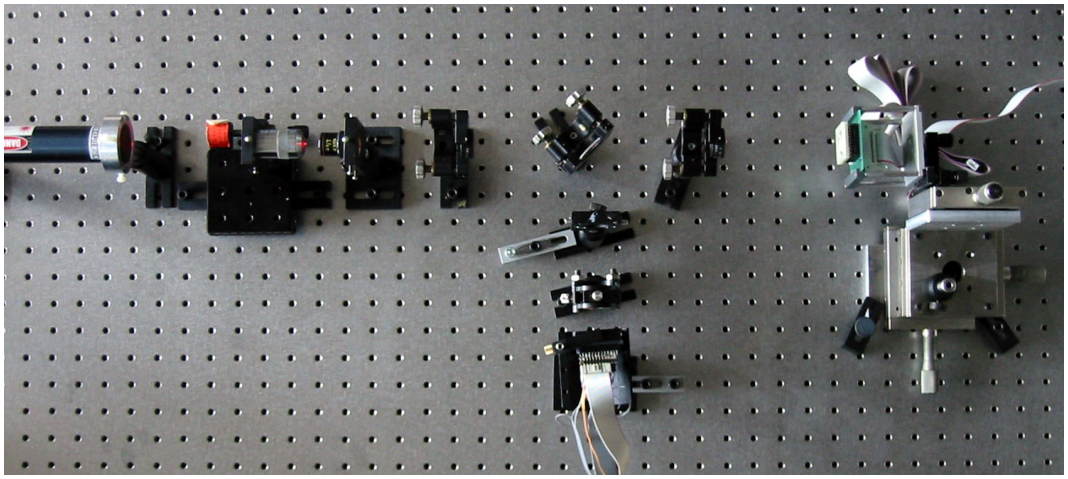

Figure 4.1: Photo of the experimental setup.

Figure 4.1 shows a photo of the complete adaptive optics system, that was implemented to test the control algorithm. I use standard optics devices and a HeNe–laser at 632.8 nm (4 mW) wavelength. The beam of the HeNe–laser is expanded to a beam waist of 8 mm. Two achromatic lenses[1] with a focal

[1]Still I use achromatic lenses, which are lens combinations, that compensate for chromatic differences, realising one single focus point for all wavelengths. But that is only because it makes no difference for monochromatic light and that they were already on stock. Besides the realisation of a diagnoses unit based on an auto fluorescence microscope runs only with a multi chromatic light source.

length of 100 mm are positioned in focal planes between the membrane mirror and the expander output. In the focus point between the lenses a beam–splitter (transmission of 30%, reflection of 70%) redirects the beam after reflection at the mirror in direction of the sensor. The beam passes another achromatic lens of only 50 mm focal length. This halves the beam diameter before it is incident upon the lenslet array and the HSS asic. The expander output, the mirror and the lenslet array are positioned in conjugated planes.

4.1.2 Hartmann-Shack Sensor

The sensor I use to detect spot positions is a Hartmann–Shack type sensor, which consists of a lenslet array out of 400 μm diameter micro–lenses with a focal length of 30 mm (figure 4.3) and an asic designed by Thomas Nirmaier[18]. The HSS asic, shown in figure 4.2, relies on standart CMOS[2] technology. The core with a total size of 4.08 mm×4.08 mm consists of an array of 8×8 position sensitive detectors, each matching the size of a microlens of the lenslet array. The detectors contain 21×21 $n+$/substrate photodiodes with a diameter of 7 μm, a ring–ring network of winner–take–all circuits and digital multiplexers for read–out. The chip achieves a fill factor of 80%. It is specially designed to overcome speed limitations of conventional ccd cameras and software solutions, to be used for applications in biomedical optics. The data analysis could be done

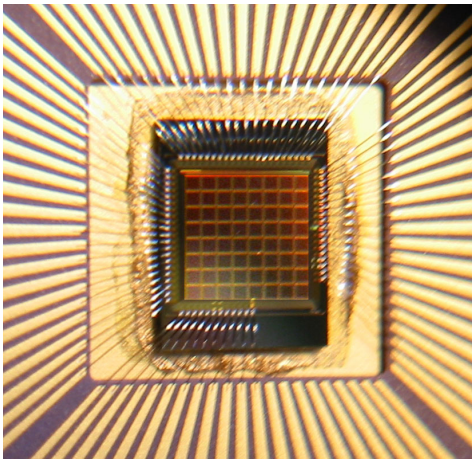

Figure 4.2: Photo of HSS asic

with a FPGA[3] directly reading out the spot positions and calculating the control signals for an adaptive mirror, to realise a real time closed–loop adaptive optics system. For the evaluation of the HSS asic's performance T. Nirmaier chose a

[2]CMOS is the abbreviation for Complementary Metal Oxide Semiconductors
[3]FPGA is the abbreviation for Field Programmable Gate Array

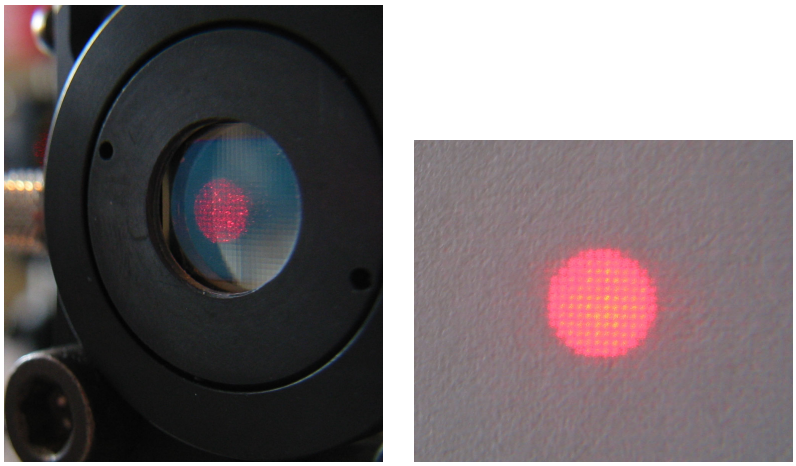

(a) (b)

Figure 4.3: Photo of the Lenslet array (a) and a spot pattern derived with it (b).

simpler variant, which I use for my first tests. Over a PCI–based data acquisition card ME–2600 from Meilhaus, containing four D/A and four A/D converters as well as two 16–bit digital ports, that can be programmed as input and output ports separately, a C++ programm communicates with the sensor. Forming the reconstruction unit of the system, it computes the first 14 Zernike coefficients, out of the 8×8 spot positions and allows repetition rates in the range of 1 kHz. The Zernike coefficients are represented in the Malacara notation, which has been described in chapter 2.

4.1.3 Membrane Mirror

The correction device is a 37-channel micro-machined deformable mirror system designed and produced by OKO Thechnologies (technical passport see [24], picture see figure .4.5). A photo is shown in figure 4.5. It consists of a silicon nitride membrane of 15 mm diameter, coated with aluminum. The maximum optical load it tolerates for λ =632.8 nm cw, is 0.03 W/mm^2. Underneath 37 close-packed hexagonal control electrodes are positioned within a circle of 12 mm diameter (see figure 4.4). Their center-to-center distance amounts to 1.75 mm. The maximal voltage the mirror abides is 250 V between actuator and membrane, which limits the maximum deflection of the whole system.

Interferometer

To measure the voltage response behaviour of the membrane mirror surface I used a μPhase Interferometer from FISBA OPTIK AG (see figure 4.6). It is based on a Twyman–Green system, which is a Michelson–Interferometer for collimated

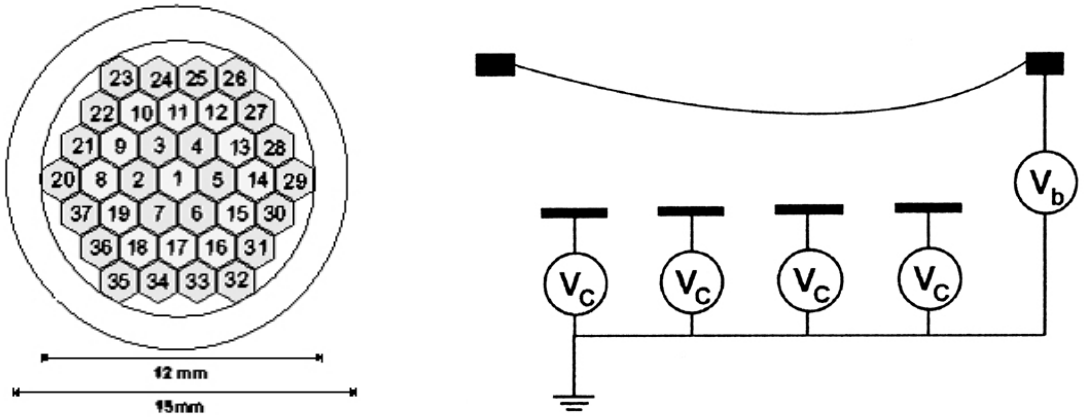

(a) (b)

Figure 4.4: The hexagonal structure of the electrodes (a) and a section through the mirror, where the electrodes and the membrane can be seen (b).

light. The light source is an external highly stabilised HeNe–laser (λ =632.8 nm), launched by a fiber. An internal ccd–camera digitises the fringe pattern and a software, from FISBA OPTIK AG, analyses the phase–shifts.
I used μShape 3.11, which is the latest freely available version. It can calculate directly the Zernike polynomials till the 35th order in ISO nomenclature out of the data of a measured surface.

4.1.4 Digital Analog Converter

The computer interface is a D/A converter specially designed for this application by Lothar Bockstaller GmbH. It is an ISA bus plug–in card with 4 times 40 channels, each susceptive to 13 bit words. The channels' output voltage ranges from -5 V to 5 V. A cycle of setting all 40 channels takes 1.3 ms, viz the DAC card allows an update frequency of 770 Hz.
To access the card I used the freely available MapMemPlus driver, a universal Windows NT driver designed by the Ecole d'ingénieurs du Canton de Vaud.

4.1.5 Amplifier Board

As it needs higher voltages, than those 5 V from the DAC card, to drive the mirror, A. Türpitz, a former group member, has designed a board to amplify the DAC signal by a constant factor[4] (see also [5]). To drive all of the mirror

[4]The amplification factor is ~ 53 and the rise time of 220 μs does not affect the performance of the servo loop.

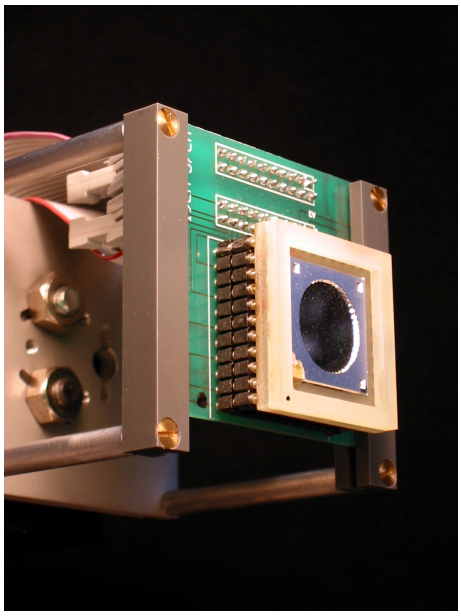

Figure 4.5: Photo of the membrane mirror clamped to its holder.

electrodes two boards are involved, each connected to 19 actuators, central and peripheral ones respectively. According to [25] the quality of the output voltage depends mainly on the high voltage source used, which in this setup is a Rhode & Schwartz power supply.

4.2 Control Algorithm

An important part of the adaptive optics system is the algorithm, that translates the reconstructed surface into signals for the control unit. In this implementation translation means finding the voltage distribution for the actuators of the membrane mirror.
Working with the same active mirror Stephan Wühl, a former member of this group, compared the performance of a control sequence based on a genetic algorithm with one working sequentially[25]. The primer takes an arbitrary voltage distribution for all actuators as a starting matrix, optimising it evolutionary. This means that the evolutional algorithm compares the (n-1) wavefront with the current and changes maximally all actuators. The latter changes the voltages sequentially, i.e. addressing one actuator after the other, to find the best fitting voltage distribution. S. Wühl came to the conclusion, that the genetic algorithm needs fitting parameters, which are not trivial to define, but a further analysis of this problem could lead to a high quality of correction. Whereas the sequential approach has some principle problems to cope with the crosstalk of the electrodes,

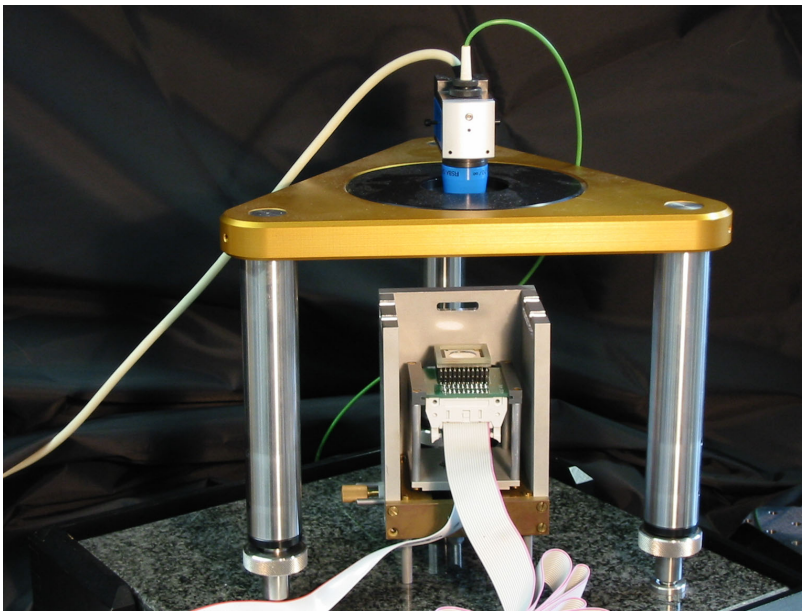

Figure 4.6: The mirror mounted underneath the interferometer.

he did not see a solution for. But both are not suitable for real time corrections, as they need at least some hundred wavefront measurements to correct for one static aberration.
As a high frequency of correction is the aim of this adaptive optics system to be implemented, it would be preferable to find a direct way to calculate the voltage distribution for the actuators out of the reconstructed Zernike coefficients, instead of optimising this distribution successively in many measurements. So I choose a linear approach, i.e. a linear approximation of the 'answering behaviour' of the mirror. The idea is to describe any mirror surface as a linear superposition of certain basic modes. A basic mode of the mirror is the surface generated by the deflection due to a single electrode charged to the mean value, whereas all other electrodes remain grounded. If for each of those basic surfaces the control voltage for every actuator is known, then the voltage distribution of any surface can be found by simple linear transformations.
As the membrane is clamped to the holder at its edge, the stroke of the outer elements is damped notably. Therefore I constrict the wavefront onto the inner part of about 8 mm of diameter and approach only the first 19 actuators, that are the center element and the first two rings. Thus to control the mirror I get 19 degrees of freedom, i.e. 19 basic modes. To determine the basic modes experimentally I take the response–surface for each actuator driven with 100 V, while

the rest of the actuators as well as the membrane are grounded.

$$\vec{U}_i = \begin{pmatrix} 0 \\ . \\ . \\ 100\text{V} \\ . \\ . \\ 0 \end{pmatrix} \leftarrow ith\ element \quad \Rightarrow \quad \vec{S}_i = \begin{pmatrix} c_1 \\ . \\ . \\ . \\ . \\ . \\ c_{19} \end{pmatrix}, \ i = 1, \ldots, 19, \tag{4.1}$$

where S_i is the vector of Zernike coefficients representing the measured surface i in the accuracy of 19 Zernike polynomials. I left out piston as it is a constant term, a shift of the complete wavefront and not measurable with a Hartmann–Shack sensor, so that the coefficients in the vector belong to the Zernike polynomials C1 till C19. I have chosen the voltage of 100 V here because it is close to the mean voltage, that can be applied to the mirror (see 4.4.1).
Any surface can then be represented in terms of this bases as matrix multiplication of a specific surface–coefficient–vector $\vec{x}$ with a matrix A with columns of basic surfaces:

$$\vec{S}_{arbitrary} = x_1\vec{S}_1 + \ldots + x_{19}\vec{S}_{19} = \begin{pmatrix} x_1 c_{0\,1} + \ldots + x_{19} c_{0\,19} \\ . \\ . \\ . \\ x_1 c_{19\,1} + \ldots + x_{19} c_{19\,19} \end{pmatrix} \tag{4.2}$$

$$\vec{S}_{arbitrary} = \underbrace{\left(\left(\vec{S}_1\right) \ldots \left(\vec{S}_1\right)\right)}_{A} \cdot \vec{x}. \tag{4.3}$$

Thus by matrix inversion I derive a prescription to specify the surface–coefficient–vector to a certain mirror surface,

$$\vec{x} = A^{-1} \cdot \vec{S}_{arbitrary}, \tag{4.4}$$

where the x_i specify how much of a certain basic surface i is needed. As will be seen later on (figure 4.9), the correlation of voltage and stroke is quadratic. Hence voltage that must be applied to electrode i to maintain a mirror surface like $\vec{S}$ is:

$$v_i = \sqrt{x_i} \cdot 100\text{V}. \tag{4.5}$$

That means, finding the control voltages, to rebuild a given surface with the membrane mirror, can be approximated by one single matrix multiplication. This makes the linear approach superior to the approaches described above, where several hundred iterations were required to obtain a corrected wavefront. The quality of correction due to the linear approach is discussed in section 4.4.2.

4.2.1 'Normalised' Surface–Vectors

To guaranty, that the symmetry of the mirror actuators is reproduced by the matrix, I normalise the 19 basic modes to form unity modes. As the actuators are positioned symmetrically around a center actuator, stimulating the third actuator should result in the same surface as stimulating the second, only turned by 30°. Hence I turn all surfaces measured for the stimulation of the elements of the first and second ring to superimpose with the stimulation of the second respectively eights actuator. Then I calculate the average surface and rotate this back into the different initial positions. A sketch of the mirror elements to illustrate the rotation is given in figure 4.7.

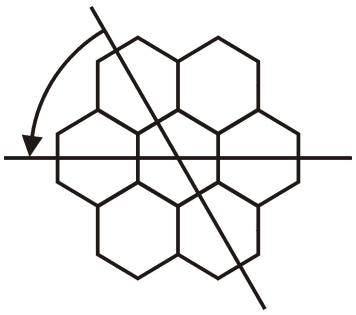

Figure 4.7: Sketch of the mirror elements with a rotation–angle.

Surface $\vec{S}_i$ rotated by the angle ϕ is:

$$\vec{S}_{rotated}(\phi, \vec{S}_i) = \begin{pmatrix} c_1\cos(\phi) + c_2\sin(\phi) \\ c_2\cos(\phi) - c_1\sin(\phi) \\ c_3 \\ c_4\cos(2\phi) + c_5\sin(2\phi) \\ c_5\cos(2\phi) - c_4\sin(2\phi) \\ c_6\cos(\phi) + c_7\sin(\phi) \\ c_7\cos(\phi) - c_6\sin(\phi) \\ c_8 \\ c_9\cos(3\phi) + c_{10}\sin(3\phi) \\ c_{10}\cos(3\phi) - c_9\sin(3\phi) \\ c_{11}\cos(2\phi) + c_{12}\sin(2\phi) \\ c_{12}\cos(2\phi) - c_{11}\sin(2\phi) \\ c_{13}\cos(\phi) + c_{14}\sin(\phi) \\ c_{14}\cos(\phi) - c_{13}\sin(\phi) \\ c_{15} \\ c_{16}\cos(\phi) + c_{17}\sin(4\phi) \\ c_{17}\cos(\phi) - c_{16}\sin(4\phi) \\ c_{18}\cos(3\phi) + c_{19}\sin(3\phi) \\ c_{19}\cos(3\phi) - c_{18}\sin(3\phi) \end{pmatrix}, \; i = 2, \ldots, 7, \tag{4.6}$$

c_i: Zernike coefficients of the surface $\vec{S}_i$
The average surface then is:

$$\vec{S}_{\emptyset} = \frac{1}{6}\sum_{i=2}^{7} \vec{S}_{i,rotated}. \tag{4.7}$$

4.3 Software Implementation

As mentioned before the spot pattern is analysed on a Linux machine using a Linux driver for the HSS I/O–board and the mirror control program runs on a Windows machine using a windows driver for the mirror's I/O–board. It would need a new driver and therefore a new program to run the HSS asic under Windows or the mirror under Linux. This should be the next step, to implement a fast time adaptive optics system, but can't be done within the scope of this work. My priority is to test an algorithm, which is highly suitable for real time applications, in the first place and not so much to optimise the time performance of any exiting adaptive optics system. So I use the local–area–network (LAN) to transfer the data from the HSS to the mirror. The program to interface the mirror is realised in C++, it is a strict object orientated implementation. The code itself and the user interface are machine and operating system independent[5], which makes them ideally suited for portation. The calculation of the control voltages, with the algorithm described above, is easily implemented and does not represent a dominating time factor on any of today's computers. Especially as it can be optimised to any given hardware, or be implemented on a FPGA board.
The user interfaces of the sensor– as well as the mirror–control are shown in figure 4.8. Most area of the sensor control interface is occupied by a spot patter, representing the 8×8 sensors of the asic. The red dots give the measured positions of the focus points. The size is the same for all points and does not correspond to the actual point sizes. Due to stray light some of the sensors can not determine a unique spot, hence do not report one. However the wavefront surface can be evaluated, using an interpolation between the remaining spots. In the lower part of the interface, the Zernike coefficients are represented in a bar plot. This starts with the Z_3 according to the Malacara notation and goes up to Z_{14}.
The mirror control interface is implemented to go in a sigle step mode through the iterations of the servo loop. For each step the different potentials at each actuator are listed in the lower right part. In the control sequence error messages such as >>`potential limit at actuator` A_i `reached`<< are reported.

[5]Current restriction is the lack of a suitable hardware driver for the I/O–boards on every operating system.

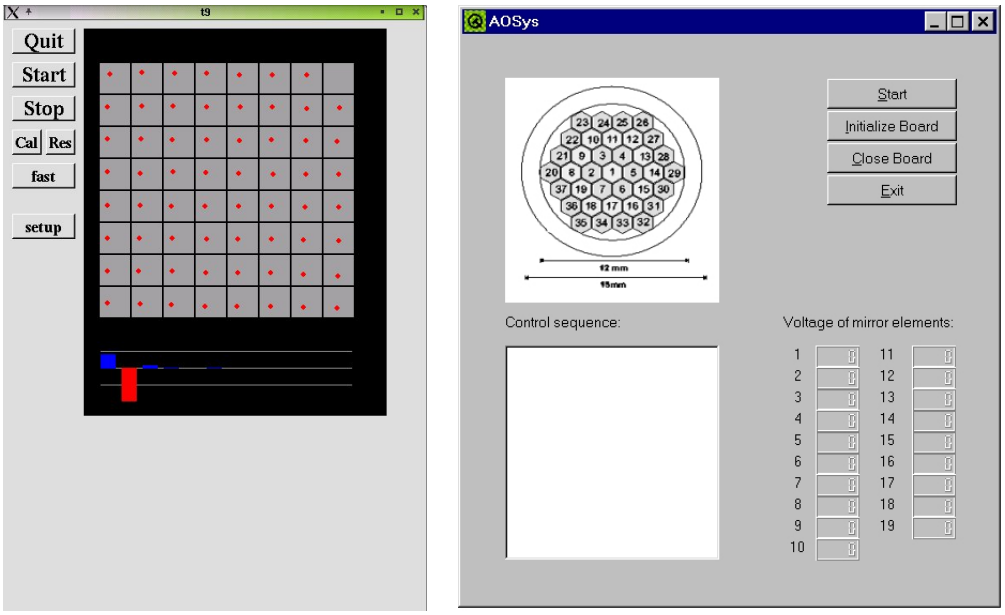

(a) (b)

Figure 4.8: The user interface to control the sensor (a) and the mirror (b).

4.4 First Measurements

4.4.1 Surface Measurements with Interferometer

In neutral position, i.e. without any voltage applied, the membrane mirror shows a relatively strong defocus with a peak–to–valley (P–V) deviation of flat less than 1.2 μm, which is twice the magnitude observed by A. Türpitz for the same mirror in 2000. This is probably an effect of aging or bad treatment as well as, that the maximum P–V value, gained for deflection of the center element by applying the maximum voltage of 250 V, while the rest is grounded, of about 1.06 $\lambda = 68.64$ nm is only 10% of the value obtained by A. Türpitz. The membrane might have lost some of its flexibility.
To control the membrane's shape by applying voltages the most important magnitude is the correlation between voltage and stroke. For the first element it can be seen in figure 4.9. The best fit is a quadratic relation, hence I implemented it in my algorithm as mentioned before (section 4.2).
Also quadratic in first approximation is the coefficient–voltage correlation, which is illustrated for the first 8 Zernike coefficients in figure 4.10.

To motivate a linear approach I made some measurements concerning the crosstalk between neighboured actuators. Therefore I applied different voltages between 0 V and 200 V to the center element, then to the second and at last simultaneously to both. I compared the coefficients measured for the simultaneous

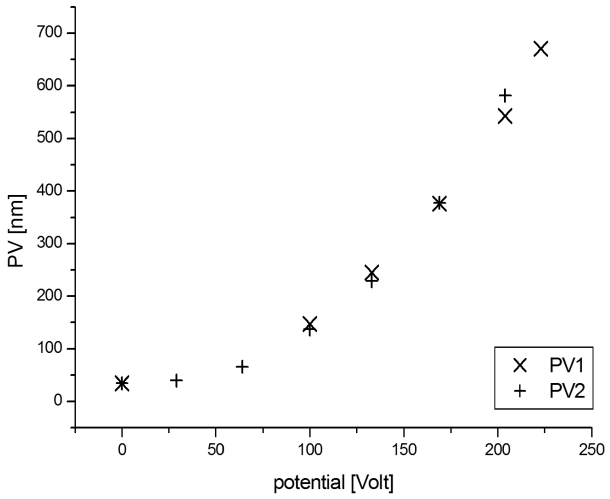

Figure 4.9: Correlation between applied Potential and maximal stroke.

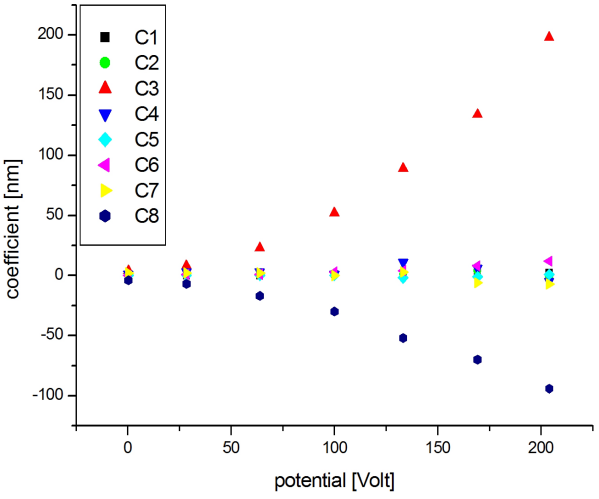

Figure 4.10: Correlation between applied potential and the different Zernike coefficients for the center actuator.

stimulation with coefficients derived by adding up the coefficients of the surfaces for separately stimulated actuators. As can be seen in table 4.1 (see also figure 4.11) for the case of 100 V applied to the center element and 150 V to the second actuator, despite the crosstalk between neighbours the actuator activities can be approximated with a linear fit. Especially for a closed loop system this should be adequate, as all deviations are re–corrected continuously.

C_i	$S_1[nm]$	$S_2[nm]$	$S_3[nm]$	S_1 + S_2[nm]	deviation[nm]
C_1	-1	21	24	20	4
C_2	1	3	5	4	1
C_3	45	40	82	85	3
C_4	3	-63	-58	-60	2
C_5	1	-16	-18	-15	3
C_6	-17	-58	-75	-75	0
C_7	-9	-8	-17	-17	0
C_8	-23	5	-20	-18	2
C_9	-3	37	32	34	2
C_{10}	-3	10	10	7	3
C_{11}	-2	42	35	40	5
C_{12}	2	12	12	14	2
C_{13}	17	-2	13	15	2
C_{14}	4	-4	4	0	4
C_{15}	10	-2	8	8	0
C_{16}	8	-13	-2	-5	3
C_{17}	4	-7	-3	-3	0
C_{18}	-3	-24	-28	-27	1
C_{19}	-1	-10	-10	-11	1

Table 4.1: S_1 is the surface measured for applying 100 V to the first actuator, for 150 V applied to the second actuator S_2 is measured. S_3 is the surface corresponding to those voltages both applied at the same time and in the fourth column the sum of the first two surfaces is listed. The last column gives the deviation of the added surface to S_3 for each Zernike coefficient. The mean deviation is 2 nm.

The 19 basic surfaces were measured with the interferometer in a unbiased

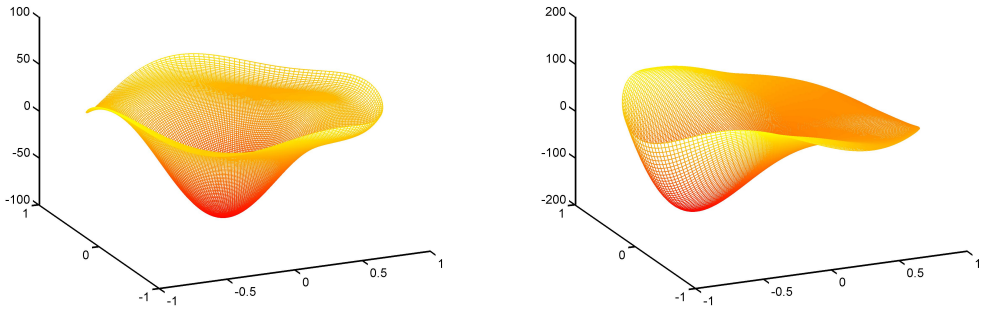

(a)

(b)

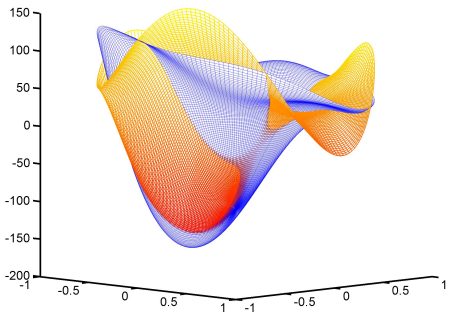

(c)

Figure 4.11: Mirror surface with 100 V applied to the center element (a) and with 150 V applied to the second actuator (b). Measured mirror surface with 100 V applied to the center element and 150V applied to the second actuator simultaneously (red) and the mirror surface, derived by adding up coefficients of the two surfaces above (blue)(c). Generally all heights are strongly exaggerated.

configuration. United in a matrix they are:

$$A = \begin{pmatrix} 0. & 10 & 5 & -6 & -10 & -5 & 5 & 1 & 4 & 1 \\ 0 & 0 & 9 & 8 & -2 & -10 & -9 & -1 & 2 & 2 \\ 46 & 23 & 23 & 17 & 25 & 24 & 23 & 1 & 2 & 1 \\ -3 & -24 & 9 & 15 & -21 & 9 & 6 & -25 & -16 & 11 \\ 0 & -1 & -20 & 19 & -1 & -17 & 20 & 0 & -27 & -21 \\ -3 & -32 & -17 & 14 & 29 & 14 & -18 & -1 & -3 & 0 \\ -1 & -1 & -25 & -27 & -2 & 25 & 24 & -1 & -2 & -1 \\ -20 & 2 & 2 & -4 & 1 & 2 & 5 & 0 & 1 & 0 \\ 2 & 12 & -11 & 12 & -7 & 10 & -10 & 16 & 0 & -15 \\ 2 & 2 & 1 & -2 & 1 & 1 & 0 & 2 & 21 & 0 \\ -3 & 16 & -10 & -15 & 17 & -11 & -10 & -2 & 1 & 0 \\ 1 & 2 & 16 & -17 & -1 & 15 & -15 & 1 & 3 & 0 \\ -1 & 5 & 1 & -4 & -12 & -5 & 3 & 0 & -2 & -1 \\ -1 & -2 & 4 & 0 & -2 & -8 & -9 & -2 & -3 & -2 \\ 14 & -2 & -1 & 4 & -4 & -2 & -2 & 1 & 2 & 1 \\ -1 & -6 & 1 & 4 & -5 & 2 & 4 & -11 & 7 & 5 \\ 0 & -1 & 6 & -4 & 0 & 4 & -4 & 0 & -10 & 10 \\ -1 & -12 & 9 & -12 & 9 & -11 & 10 & -1 & -1 & 0 \\ 3 & 1 & 1 & 3 & 1 & -1 & 2 & 1 & -3 & 1 \end{pmatrix} \ldots$$

$$\begin{pmatrix}
0 & -1 & -5 & -2 & -3 & -1 & 0 & 1 & 4 \\
5 & 2 & 2 & -1 & 0 & 0 & -4 & -2 & -2 \\
2 & 2 & 3 & 1 & 5 & 2 & 5 & 1 & 2 \\
32 & 9 & -15 & -23 & -16 & 9 & 26 & 8 & -17 \\
-1 & 19 & 25 & -1 & -25 & -19 & 2 & 20 & 24 \\
0 & -1 & 2 & -1 & 4 & -1 & -1 & 0 & -4 \\
-5 & -1 & -2 & -1 & 1 & -1 & 2 & 0 & 2 \\
-5 & 4 & 1 & 0 & 8 & 5 & 4 & 0 & 2 \\
0 & 17 & 2 & -14 & 3 & 17 & -1 & -14 & 3 \\
-20 & 0 & 19 & 0 & -16 & 3 & 20 & -2 & -20 \\
-5 & 0 & 2 & -1 & 1 & -1 & -4 & -1 & 1 \\
0 & 0 & -3 & 0 & 3 & 0 & 0 & 0 & -4 \\
-3 & -2 & -1 & -2 & -2 & -2 & -1 & -1 & -4 \\
-9 & -1 & -2 & -1 & -4 & -3 & 0 & 1 & 3 \\
7 & -1 & 0 & 0 & -3 & 0 & -1 & 1 & 0 \\
-13 & 4 & 6 & -11 & 7 & 5 & -13 & 7 & 5 \\
1 & -10 & 11 & 0 & -11 & 10 & -1 & -8 & 12 \\
0 & 0 & -1 & 0 & 0 & -1 & 0 & 1 & 0 \\
7 & 1 & -4 & 0 & 5 & 0 & -5 & -1 & 3
\end{pmatrix}$$

where each column corresponds to one surface, listing its coefficients C1 till C19.

This is the basic matrix first implemented in the control algorithm. But measurements showed some problems with the astigmatic term (see section 4.4.2), so that I averaged this matrix to fit the actuators symmetry. The matrix I derived out of this 'normalisation', according to the normalisation procedure described above, is:

$$A_{normal} = \begin{pmatrix}
0 & 10. & 4.6 & -5.7 & -10. & -4.6 & 5.7 & -6.0 & -5.3 & -5.1 \\
0 & 0.64 & 9.2 & 8.6 & -0.64 & -9.2 & -8.6 & 0.29 & -2.8 & 3.3 \\
46. & 23. & 23. & 23. & 23. & 23. & 23. & 4.5 & 4.5 & 4.5 \\
-3.0 & -22. & 11. & 11. & -22. & 11. & 11. & -52. & -25. & -27. \\
0 & -0.067 & -19. & 19. & -0.067 & -19. & 19. & -0.93 & -46. & 45. \\
-3.0 & -30. & -15. & 15. & 30. & 15. & -15. & 3.6 & 3.2 & 3.0 \\
-1.0 & 0.11 & -26. & -26. & -0.11 & 26. & 26. & -0.14 & 1.7 & -1.9 \\
-20. & 1.3 & 1.3 & 1.3 & 1.3 & 1.3 & 1.3 & 3.3 & 3.3 & 3.3 \\
2.0 & 10. & -10. & 10. & -10. & 10. & -10. & -35. & 2.0 & -2.0 \\
2.0 & -0.17 & 0.17 & -0.17 & 0.17 & -0.17 & 0.17 & -2.0 & -35. & 35. \\
-3.0 & 18. & -8.9 & -9.5 & 18. & -8.9 & -9.5 & 3.5 & 1.5 & 1.9 \\
1.0 & -0.33 & 16. & -16. & -0.33 & 16. & -16. & 0.23 & 3.1 & -2.9 \\
-1.0 & 6.9 & 3.1 & -3.8 & -6.9 & -3.1 & 3.8 & 1.9 & 2.2 & 1.1 \\
-1.0 & 0.39 & 6.2 & 5.8 & -0.39 & -6.2 & -5.8 & -1.0 & 0.061 & -1.8 \\
14. & -1.2 & -1.2 & -1.2 & -1.2 & -1.2 & -1.2 & 1.2 & 1.2 & 1.2 \\
-1.0 & -5.3 & 1.8 & 3.6 & -5.3 & 1.8 & 3.6 & -24. & 13. & 11. \\
0 & -1.1 & 5.2 & -4.1 & -1.1 & 5.2 & -4.1 & -0.91 & -20. & 21. \\
-1.0 & -10. & 10. & -10. & 10. & -10. & 10. & 5.0 & 0.67 & -0.67 \\
3.0 & -0.17 & 0.17 & -0.17 & 0.17 & -0.17 & 0.17 & -0.67 & 5.0 & -5.0
\end{pmatrix} \ldots$$

$$\begin{pmatrix}
-3.3 & -2.8 & -0.29 & 0.29 & 2.8 & 3.3 & 5.1 & 5.3 & 6.0 \\
-5.1 & 5.3 & -6.0 & 6.0 & -5.3 & 5.1 & -3.3 & 2.8 & -0.29 \\
4.5 & 4.5 & 4.5 & 4.5 & 4.5 & 4.5 & 4.5 & 4.5 & 4.5 \\
27. & 25. & 52. & 52. & 25. & 27. & -27. & -25. & -52. \\
-45. & 46. & 0.93 & 0.93 & 46. & -45. & 45. & -46. & -0.93 \\
1.9 & 1.7 & 0.14 & -0.14 & -1.7 & -1.9 & -3.0 & -3.2 & -3.6 \\
3.0 & -3.2 & 3.6 & -3.6 & 3.2 & -3.0 & 1.9 & -1.7 & 0.14 \\
3.3 & 3.3 & 3.3 & 3.3 & 3.3 & 3.3 & 3.3 & 3.3 & 3.3 \\
35. & 35. & -2.0 & 2.0 & -35. & -35. & 2.0 & -2.0 & 35. \\
2.0 & 2.0 & 35. & -35. & -2.0 & -2.0 & -35. & 35. & 2.0 \\
-1.9 & -1.5 & -3.5 & -3.5 & -1.5 & -1.9 & 1.9 & 1.5 & 3.5 \\
2.9 & -3.1 & -0.23 & -0.23 & -3.1 & 2.9 & -2.9 & 3.1 & 0.23 \\
1.8 & 0.061 & 1.0 & -1.0 & -0.061 & -1.8 & -1.1 & -2.2 & -1.9 \\
1.1 & -2.2 & 1.9 & -1.9 & 2.2 & -1.1 & 1.8 & -0.061 & 1.0 \\
1.2 & 1.2 & 1.2 & 1.2 & 1.2 & 1.2 & 1.2 & 1.2 & 1.2 \\
11. & 13. & -24. & -24. & 13. & 11. & 11. & 13. & -24. \\
21. & -20. & -0.91 & -0.91 & -20. & 21. & 21. & -20. & -0.91 \\
-5.0 & -5.0 & -0.67 & 0.67 & 5.0 & 5.0 & 0.67 & -0.67 & -5.0 \\
0.67 & 0.67 & -5.0 & 5.0 & -0.67 & -0.67 & 5.0 & -5.0 & 0.67
\end{pmatrix}$$

On this the latest version of the control algorithm is based. As is shown in the

next section, the astigmatic aberrations do not increase so strongly anymore using this 'normalisation'.

4.4.2 Wavefront Corrections with Adaptive Optics System

After the matrices have been determined using the interferometer the mirror is introduced into the adaptive optics setup. Initially the system is aligned in such a way, that the Hartmann–Shack sensor measures zero for all coefficients, i.e. the system is calibrated. This is done while no control voltage is applied to the mirror. In a pre biased configuration the mirror would be at the bias voltage. Correction of defocus, astigmatism and a combination of both, has been realised till now.
I start testing the plane inverse of the measured matrix, the 'un–normalised' one. A defocus is to be corrected, which I obtain by adjusting one part of the beam expander out of focus. In figure 4.12 can be seen how a defocus of 0.029 nm can be decreased to a value of only 0.006 nm. Within three iterations the magnitude of defocus converges to its final value, hence the iteration can be stopped. The final value is determined due to the maximum deflection of the mirror's membrane (0 V, 250 V). However, figure 4.12 shows, that the astigmatism 0° grows with each iteration. This astigmatism must be inherent in the measured matrix. As can be seen by the following measurements, this is no principle problem of the approximation, but due to inaccuracies of the surface measurements, on which the matrix is based. The symmetrical relations within the matrix correspond only insufficiently to the actuator symmetry. Therefore I made the effort of normalising the matrix input. Using the normalised matrix I again correct for different magnitudes of defocus and astigmatism. The defocus is illustrated in figur 4.13. A defocus of 0.04 nm converges to 0.015 nm already after the first iteration. The astigmatism 0° still increases as in the un–normalised case, but it settles at a lower value of 0.02 nm.
This shows, that the normalisation improves the approach. However, not all residual errors can be corrected. A more detailed discussion of the remaining errors can be found in section 4.4.2. Furthermore I perform measurements to analyse the capability of the adaptive optics system to corrector for first order astigmatism (0° and 45°) as well as combinations of defocus and astigmatism. In addition the behaviour of the major contributing terms are observed.
An astigmatism 45° of 0.038 nm is decreased to its final value of 0.016 nm in only one iteration. At the same time the astigmatism 0° increases, but only to a value of -0.001 nm, that stays stable during further iterations(figure 4.14). The best result is gained for the correction of the astigmatism 0° (see figure 4.15). The astigmatism of -0.046 nm converges to the tenth of its initial value within four iterations. In addition a wavefront aberrated by a combination of defocus

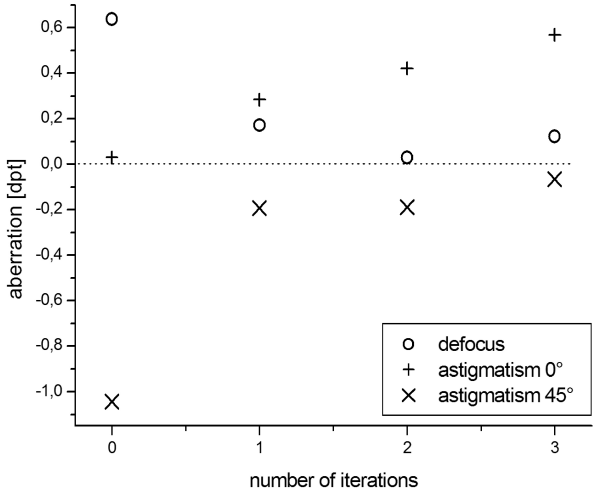

Figure 4.12: Correction of defocus with initially measured matrix.

and astigmatism 45° was corrected. I gained a decrease from 0.025 nm to a value under 0.01 nm after one iteration for the defocus. The astigmatism 45° with an initial value of 0.029 nm converges to 0.015 nm in three iterations. The astigmatism 0° increases, but only till it reaches a value of -0.01 nm (illustrated in figure 4.16). The final value, i.e. the limit of correction, is set by the limited deviation possible of the membrane.

Critical Discussion

The first surface measurements where made with the interferometer. Therefore a special mount for the mirror was constructed by former group members. The position in the planar directions can be fine tuned with micrometer screws. The tilt can be compensated by tilting the interferometer itself via fine screws. The position of the mirror has to be precisely adjusted with respect to the interferometer. As the Zernike polynomials are evaluated on a unit circle, this circle's center has to correspond to the mirror center. To assure a good alignment the following procedure is performed. First the central actuator is deflected to the maximum value. This should result in a leading defocus term and especially no tilt should be present. Now the mirror's position is adjusted until the tilt coefficients are minimised. A zero for both tilt terms is hardly reachable with this setup. Obviously this leads to systematic errors, when the Zernike coefficients are evaluated.
The described linear approach is founded on the possibility to have precise measurements of the basic modes. Any error occurring in the determination of those

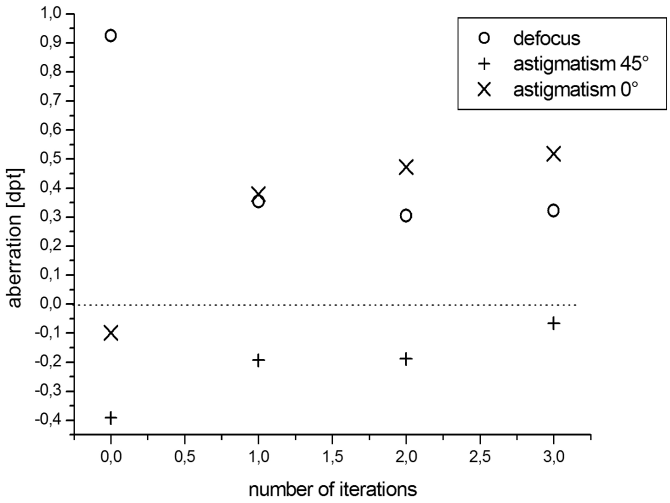

Figure 4.13: Defocus correction with the normalised matrix.

basic modes, due to systematic misalignment which affects all Zernike coefficients, can not be removed by normalisation of the surface matrix, but propagate through to the control instructions of the servo loop.
Now I will focus on the adaptive optics system itself. Adjusting this system several sources for image errors occur. Again the positioning of mirror is crucial. The mirror center has to be exactly on the optical axis. To assure a good alignment I employed x–y–z–translation stage as well as a tip–tilt stage in two directions. It is possible to do a pre alignment observing the beam trail. The tip–tilt alignment can be done by superimposing incoming and reflected beam. The fine adjustment is achieved by using the HSS asic. However, the wavefront detector has an intrinsic error source itself.
As mentioned before the detector consists of the lenslet array and the HSS asic. These two components have to be aligned in such a way, that every sensor of HSS asic is illuminated by a single lens. The lenslet array is matched to the geometry of the HSS asic only if the rows of lenslets are parallel to the sensor rows and at focal distance. As the correct distance can easily be assured, as main error source remains the rotational degree of freedom. The right angular position for the lenslet can be found by exposing the HSS asic to a planar wave. Summarising, the HSS asic is adjusted correctly if, exposed to a planar wave, it detects a planar wave. The errors due to rotational misalignment have been elaborately discussed in [25].
Errors due to the mechanical properties of the mirror itself, as they are degraded flexibility of the membrane as well as finite deflection possible, are mentioned

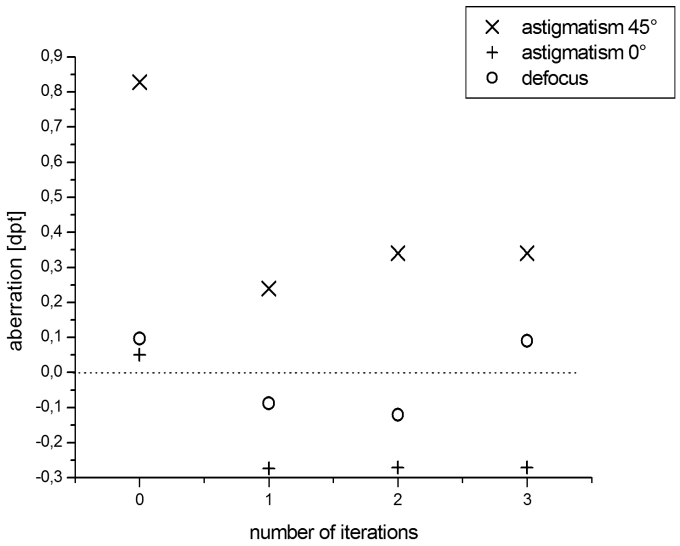

Figure 4.14: Correction for astigmatism 45° with the normalised matrix.

within previous sections.
Further error sources, which arise from the design of the HSS asic are discussed in [18].

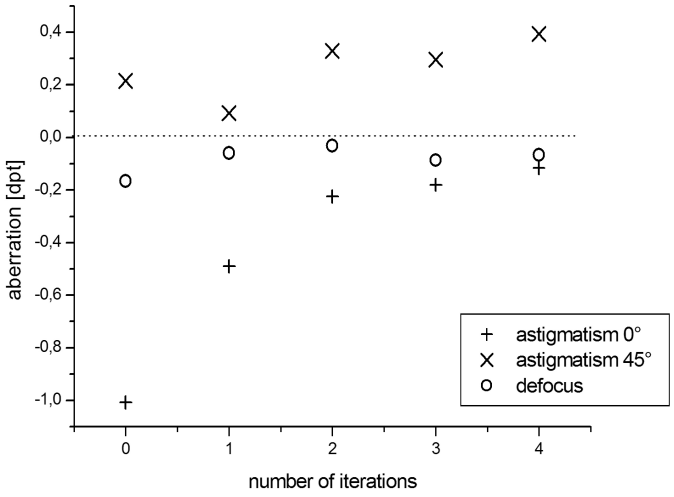

Figure 4.15: Correction for astigmatism 0° with the normalised matrix.

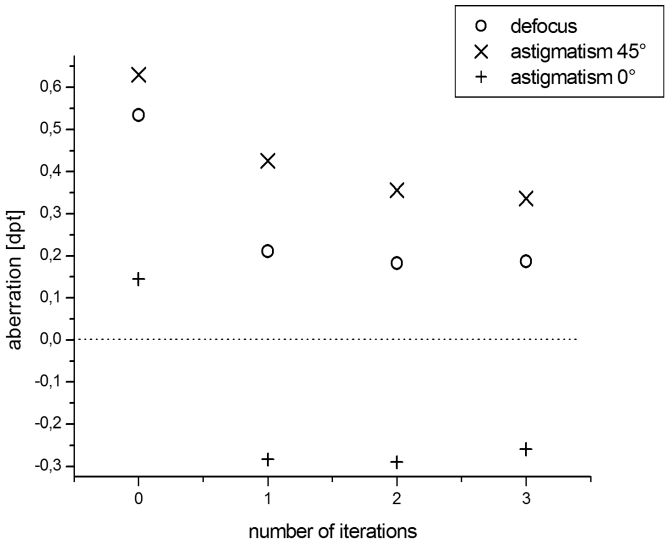

Figure 4.16: Correction for a combination defocus and astigmatism 45°.

Chapter 5

Conclusion

In this diploma thesis it could be shown, that a linear approach to control a membrane mirror has a high potential for real time realisations of adaptive optics systems. The linear approximation of the mirror response to applied voltages enables a correction of common aberrations within one to three iterations, i.e. one to three times measurement and reconstruction of the wavefront as well as adjustment of the mirror. In contrast to the earlier (in this group) tested approaches this makes it realistic to reach frequency ranges for wavefront correction of several kHz implemented in an appropriate system.
The aberrations decreased to values between 10 and 50 % of their original size. Those limits were set by the flexibility of the membrane mirror. As the mirror used in the adaptive optics system implemented to test the algorithm seems to have lost great amount of its flexibility, a fully working mirror should increase the extent of correction significantly.
Another limit for the quality of correction represent the basic modes employed in the control algorithm. As is shown, the averaging of those modes improved the algorithm's ability greatly. This emphasises the importance to account for the symmetry of the actuator's positions. Hence the optimisation of the matrix, i.e. of the quality of the surface measurements, should amend the algorithm's performance. With the here applied interferometer this could be realised by increasing the accuracy of the mirror positioning underneath the instrument. It should be centered more precisely.
An employment of the algorithm to increase the image quality of the microscope for diagnostic purposes is highly recommendable, especially as the algorithm shows a very strong converging. In comparison to the stochastic converging of the genetic algorithm, where also far off pictures are tested, this algorithm will rapidly sharpen the picture without flickering.
Using adaptive optics to control the ablation laser's focus is more problematic. A membrane is a quite sensitive feature, that can't cope with optical loads suitable to cause ionisation. Till now I do not know any active device resistive to such high power densities.

Appendix A

Zernike Polynomials

The polinomial series picked for L_i is the following:

$$\begin{aligned} L_1 &= 1, \\ L_2 &= x, \\ L_3 &= y, \\ L_4 &= xy, \\ L_5 &= x^2 - y^2, \\ L_6 &= x^2 + y^2 - \alpha, \\ L_7 &= x^3 - \beta x, \\ L_8 &= \beta y - y^3, \\ L_9 &= xy^2 - \tau x, \\ L_{10} &= x^2 y - \tau y, \end{aligned}$$

within the accuracy of the 3rd order, i.e. up to L_{10} and with

$$\begin{aligned} \alpha &= \frac{2\sum_{n=1}^{N} x_n^2}{N}, \\ \beta &= \frac{\sum_n x_n^4}{\sum_n x_n^2}, \\ \tau &= \frac{\sum_n x_n^2 y_n^2}{\sum_n x_n^2}. \end{aligned}$$

Coefficients k_i and l_i corresponding to the minimasation constraint are stated explicitly like:

$$k_1 = \frac{\sum_n P_n}{N},$$

$$
\begin{aligned}
k_2 &= \frac{\sum_n xP_n}{\sum_n x^2}, \\
k_3 &= \frac{\sum_n yP_n}{\sum_n y^2}, \\
k_4 &= \frac{\sum_n xyP_n}{\sum_n x^2y^2}, \\
k_5 &= \frac{\sum_n x^2P_n - \sum_n y^2P_n}{2\sum_n x^4 - \sum_n x^2y^2}, \\
k_6 &= \frac{\sum_n x^2P_n + \sum_n y^2P_n - \sum_n \alpha P_n}{2\sum_n x^4 - 2\sum_n x^2y^2}, \\
k_7 &= \frac{\sum_n x^3P_n - \beta\sum_n xP_n}{\sum_n x^6 - 2\beta\sum_n x^4 + \beta^2\sum_n x^2}, \\
k_8 &= \frac{\beta\sum_n yP_n - \sum_n y^3P_n}{\sum_n x^6 - 2\beta\sum_n x^4 + \beta^2\sum_n x^2}, \\
k_9 &= \frac{\sum_n xy^2P_n - \tau\sum_n xP_n}{\sum_n x^2y^4 - 2\tau\sum_n x^2y^2 + \tau^2\sum_n x^2}, \\
k_{10} &= \frac{\sum_n x^2yP_n - \tau\sum_n yP_n}{\sum_n x^2y^4 - 2\tau\sum_n x^2y^2 + \tau^2\sum_n x^2},
\end{aligned}
\tag{A.1}
$$

$$
\begin{aligned}
l_1 &= \frac{\sum_n Q_n}{N}, \\
l_2 &= \frac{\sum_n xQ_n}{\sum_n x^2}, \\
l_3 &= \frac{\sum_n yQ_n}{\sum_n y^2}, \\
l_4 &= \frac{\sum_n xyQ_n}{\sum_n x^2y^2}, \\
l_5 &= \frac{\sum_n x^2Q_n - \sum_n y^2Q_n}{2\sum_n x^4 - \sum_n x^2y^2}, \\
l_6 &= \frac{\sum_n x^2Q_n + \sum_n y^2Q_n - \sum_n \alpha P_n}{2\sum_n x^4 - 2\sum_n x^2y^2}, \\
l_7 &= \frac{\sum_n x^3Q_n - \beta\sum_n xQ_n}{\sum_n x^6 - 2\beta\sum_n x^4 + \beta^2\sum_n x^2}, \\
l_8 &= \frac{\beta\sum_n yQ_n - \sum_n y^3Q_n}{\sum_n x^6 - 2\beta\sum_n x^4 + \beta^2\sum_n x^2}, \\
l_9 &= \frac{\sum_n xy^2Q_n - \tau\sum_n xQ_n}{\sum_n x^2y^4 - 2\tau\sum_n x^2y^2 + \tau^2\sum_n x^2}, \\
l_{10} &= \frac{\sum_n x^2yQ_n - \tau\sum_n yQ_n}{\sum_n x^2y^4 - 2\tau\sum_n x^2y^2 + \tau^2\sum_n x^2},
\end{aligned}
$$

The resulting Taylor coefficients read as:

$$
\begin{aligned}
a_1 &= k_1 - \alpha k_6, \\
a_2 &= l_1 - \alpha l_6, \\
a_3 &= \frac{1}{2}k_2 - \frac{1}{2}\beta k_7 - \frac{1}{2}\tau k_9, \\
a_4 &= k_3 + \beta k_8 - \tau k_{10}, \\
a_5 &= \frac{1}{2}l_3 + \frac{1}{2}l_8 - \frac{1}{2}l_{10}, \\
a_6 &= \frac{1}{3}(k_5 + k_6), \\
a_7 &= l_5 + l_6, \\
a_8 &= k_6 - k_5, \\
a_9 &= \frac{1}{3}(l_6 - l_5), \\
a_{10} &= \frac{1}{4}k_7, \\
a_{11} &= l_7, \\
a_{12} &= \frac{1}{2}k_9, \\
a_{13} &= -k_8, \\
a_{14} &= -\frac{1}{4}l_8,
\end{aligned}
$$

Bibliography

[1] H.W. Babcock. The possibility of compensating astronomical imaging. *Publ. Astron. Soc. Pac.*, 56:229, 1953.

[2] D.Enard. ESO VLT Project i: a status report. *Proc. SPIE*, 1236:63, 1990.

[3] J.C.Dainty C.Paterson, I.Munro. A low cost adaptive optics system using a membrane mirror. *OPTICS EXPRESS 175 (OSA)*, 6(9), 2000.

[4] A.J.Augustin. *Augenheilkunde*. Springer, Berlin, 2001.

[5] Alexander Türpitz. PhD thesis, Universität Heidelberg, 2000.

[6] Neurozentrum Unikliniken Freiburg Abteilung Stereotaktische Neurochirurgie. *http://www.ukl.uni-freiburg.de/neurozen/stx/stereode_d.htm*.

[7] Volker Sturm Josef F.Bille, Wolfgang Schlegel. Stereotaktische Laser–Neurochirurgie. *Physik in unserer Zeit*, 6:280, 1993.

[8] M.H.Niemz. *Lasers-Tissue Interaction*. Springer-Verlag, Berlin, Heidelberg, 1996.

[9] ed. T.Wilson. *Confocal mircroscopy*. Academic Press, London, 1990.

[10] Klaus Greger. PhD thesis, Universität Heidelberg, 2003.

[11] John David Jackson. *Classical Electro Dynamics*. Wiley, New York, 1998.

[12] L.N.Thibos. *Handbook of visual optics*. 1999.

[13] Thomas E.Furtak Miles V.Klein. *Optik*. Springer–Verlag, Berlin, Heidelberg, 1988.

[14] C.Schäfer L.Bergmann. *Lehrbuch der Experimentalphysik, Bd.3, 8. Auflage*. de Gruyter, Berlin, 1987.

[15] R.K.Tyson. *Principles of Adaptive Optics*. Academic Press, London, 1991.

[16] Joseph M. Geary. *Introduction to Wavefront Sensors*. SPIE PRESS, Vol. TT 18, 1995.

[17] W.Stell R.Smartt. Theory and application of point diffraction interferometers. *Japan J. Appl. Phys.*, 14:351, 1975.

[18] Thomas Nirmaier. PhD thesis, Universität Heidelberg, 2003.

[19] Frank K. Müller. PhD thesis, Diploma thesis, Universität Heidelberg, 1998.

[20] Optics Group of the Electronic Instrumentation Lab. TU Delft. *http://guernsey.et.tudelft.nl/group/project_loktev.htm.*

[21] Artal Vargas-Martin, Pietro. Correction of the aberrations in the human eye with a liquid crystal spatial light modulator: Limits to the performance. *J.Opt.Soc.Am.A*, 15(9).

[22] BSAC. Ongoing research is done in the Berkeley Sensor and Actuator Center. *http://www-bsac.eecs.berkeley.edu/.*

[23] E. M. Ellis. Low–cost Bimorph Mirrors in Adaptive Optics. *Ph.D thesis, Imperial College of Science, Technology and Medicine, London*, 1999.

[24] OKO Technologies. *http://www.ocothech.com/mirrors/technical/index.html.*

[25] Stefan Wühl. PhD thesis, Diploma thesis, Universität Heidelberg, 1999.

Erklärung:

Ich versichere, dass ich diese Arbeit selbstständig verfasst und keine anderen als die angegebenen Quellen und Hilfsmittel benutzt habe.

Heidelberg, den 31.05.2003